

Modeling Tidal Streams and Tidal Tails Around Galaxies Using Deep Wendelstein Imaging Data

JAN-NIKLAS PIPPERT ^{1,2,*} MATTHIAS KLUGE ^{1,2} AND RALF BENDER ^{1,2}

¹Max Planck Institute for Extraterrestrial Physics, Giessenbachstrasse, D-85748 Garching, Germany

²University Observatory, Faculty of Physics, Ludwig-Maximilians-Universität München, Scheinerstr. 1, 81679 Munich, Germany

ABSTRACT

From the Λ cold dark matter paradigm it is expected that galaxies merge and grow in their environments. These processes form various tidal features depending on the merger mass ratio, orbital parameters, and gas richness. We inspected 170 g -band Abell cluster observations from the 2.1 m Fraunhofer-Teleskop Wendelstein and identify 111 of such features from which we select nine streams and five tails. A fast and innovative technique was developed for determining their photometric properties. The model is a Gaussian, including higher-order moments to describe the light profile in slices perpendicular to the elongation direction. From these models, FWHM apertures are generated. The method was developed, tested, and applied on the selected features and corresponding g - and r -band data from the Legacy Survey DR10. Regarding the novel modeling approach, we can measure surface and total brightnesses with precisions of 4% and 7%, respectively. Mean stream width precision, which also translates to the mean R_e along the feature is on average within 3% uncertainty. The measured streams have on average a surface brightness of ~ 26.25 g' mag arcsec⁻² and are dimmer than the tails in our sample (~ 25.14 g' mag arcsec⁻²). We infer that the progenitors of our streams can come from dwarfs, early-type galaxies or disks, based on the streams structural parameters. Furthermore, brightnesses and colors of the streams and tails are consistent with those of galaxies that populate the red sequence in the Coma cluster within 2σ .

1. INTRODUCTION

Structures in a cold dark matter Universe with a cosmological constant Λ assemble hierarchically through the merging of smaller dark matter halos. Those potential wells bind baryonic matter, initiating star formation and creating galaxies, which contain dark matter, gas, and stars. From there, galaxies grow through the process of galaxy mergers, which dictates their morphological appearance and kinematic evolution.

Mergers are commonly classified into three categories by the mass ratios μ of the merging galaxies (e.g., Schulze et al. 2020), namely major mergers ($\mu \geq 1/4$), minor mergers ($1/10 < \mu < 1/4$), and mini mergers ($\mu \leq 1/10$). While major mergers are rarer, about three times at $z \sim 0.7$ (Lotz et al. 2011) and about two times for $0 < z < 3$ (Conselice et al. 2022), accretion of small satellites is expected to be more common. This circumstance is also supported by the luminosity function (Schechter 1976) of galaxies, where a significantly larger number of smaller galaxies is present. During the merger

process, stellar material is ejected from the system, or stripped from an infalling satellite galaxy creating faint substructures around their host galaxies, in the form of streams, shells, tails, and continuous subforms. They store information of the past evolution of the system and give valuable insights into merger histories. The classification of these features in this work is based on the definitions used among the literature (e.g., Duc et al. 2014; Bílek et al. 2020; Sola et al. 2022; Urbano et al. 2024).

Tails originate in major galaxy merger events where the contents of both partners are ejected outward. These trails can extend up to 100 kpc (Toomre & Toomre 1972). As they come from their host, they show the same properties, e.g., age, metallicity, and color if no star formation was triggered by the merger. However, depending on the type of the merging galaxies, tails can be either red or show clumps of star formation and bluer colors (Elmegreen et al. 2007) or a superposition of both (Mulia et al. 2015). Their usual appearance consists of elongated structures on each side of the galaxy, where their most prominent example is the Antennae galaxies (e.g., Lahén et al. 2018).

* jnpippert@mpe.mpg.de

Streams, on the other hand, have a different history. They are the result of a low-mass accretion (Bullock & Johnston 2005), i.e., minor merger, where a progenitor gets accreted through dynamical friction and tidal forces and consequently stripped when entering the Roche limits, where the effect is strongest at the pericentric passage. The satellite infall for this definition of streams is biased toward circular infall (Karademir et al. 2019). While the stars disperse, they trace the orbit of the progenitor (e.g., Sanders & Binney 2013), which can result in multiple loops around the host galaxy (e.g., Martínez-Delgado et al. 2008). Streams can also occur in the process of forming shells, which is favored by radial infalls (Karademir et al. 2019).

Tidal streams in and around our Galaxy are detected either via star counts and groups of stars with coherent velocities (Malhan & Ibata 2019; Koposov et al. 2023), or groups of stars with the same chemical abundances (Martin et al. 2022). The stellar streams roughly follow the orbit of their destroyed satellite (galaxy or globular cluster), i.e., tracing the host potential, and are, hence, sensitive to the total matter within the orbit, including dark matter. Techniques such as orbital integration methods (e.g., Fardal et al. 2006; Koposov et al. 2010; Price-Whelan et al. 2014) and generative models for stream formation (e.g., Bonaca et al. 2014; Gibbons et al. 2014) are developed to constrain halo potentials. A recent study by Nibauer et al. (2023) used another approach utilizing stream tracks and trial potentials to infer the flattening of the gravitational potential. An additional example is a study by Ibata et al. (2024), which used 87 streams to refine the mass model of the Milky Way. A unified collection of galactic streams and their footprints can be found in Mateu (2023).

Further examples of streams in the Local Group (McConnachie et al. 2018), the Milky Way (Belokurov et al. 2006; Ibata et al. 2021), as well as in nearby galaxies, e.g., NGC 891 (Mouhcine et al. 2010) and NGC 5128 (Crnojević et al. 2016), are found by counting stars. Resolving stellar halos and their embedded substructures, e.g., streams, allows to reach deeper surface brightnesses than we can hope to reach with integrated photometry (e.g., due to galactic cirrus).

Due to their low surface brightness (LSB), imaging extragalactic tidal features is challenging but possible, as shown by surveys like MATLAS (Duc et al. 2014; Bílek et al. 2020; Sola et al. 2022), the Stellar Stream Legacy Survey (SSLS; Martínez-Delgado et al. 2023a) and deep galaxy cluster observations (Kluge et al. 2020).

Some photometric studies of tidal streams by Martínez-Delgado et al. (2008), Chonis et al. (2011), and Román et al. (2023) exist, where surface bright-

nesses of individual examples ranging from $\sim 26 - 28 R$ mag arcsec $^{-2}$ and up to $\sim 29.5 g$ mag arcsec $^{-2}$ are measured. They obtained the surface brightness from the flux averaged inside one FWHM of a Gaussian distribution at either a collapsed representation of the stream or of a segment, which got extrapolated to the full extent of the feature. In addition, Martínez-Delgado et al. (2021) analyzed the giant stream around M104 using the maximum surface brightness instead of the FWHM method. A few stream surveys already exist. For example, Martínez-Delgado et al. (2023a) measured the surface brightnesses in the g , r , and z bands for galaxies at redshift $z \lesssim 0.02$, in many small circular apertures arranged along the feature. They reach down to $28.4 g$ mag arcsec $^{-2}$, $26.9 r$ mag arcsec $^{-2}$, and $26.5 z$ mag arcsec $^{-2}$. Another example using the same method is the one by (Miró-Carretero et al. 2023), who provides $(g - r)$ colors and g - and r -band surface brightnesses down to 28.7 and 27.98 mag arcsec $^{-2}$ respectively.

Such studies can further be used to determine the stellar populations of the streams. Again, with streams in and around the Milky Way in which single stars are resolved, spectral classes, ages, and metallicities for each star can be obtained from the data directly. For those with an extragalactic origin, sufficiently deep spectra require long integration times and can be limited by systematics such as sky removal or continuum calibration. Therefore, one has to rely on flexible stellar population synthesis models (Laine et al. 2016), colors (Foster et al. 2014), integrated surface photometry (Martínez-Delgado et al. 2023b), or SED fitting (Laine et al. 2024).

With the launch of the Euclid space telescope, on 2023 July 1 (EUCLID; Scaramella et al. 2022), and upcoming deep optical surveys such as LSST with the Rubin Observatory (Ivezić et al. 2019) or the Nancy Grace Roman Space Telescope (Akeson et al. 2019), a highly increased number of detected LSB structures is expected. Methods relying on manual inspection will not be feasible to statistically study the properties of tidal features in galaxy groups, galaxy clusters, or around field galaxies. In this work, we focus on streams and tails and present the first automated method to create robust and precise models from deep images. The models, based on Gaussian distributions, including higher-order Hermite basis functions, generate photometric apertures defined by an FWHM criterion. In such a manner, the brightness, colors, and shape parameters of streams and tails are obtained automatically.

Our novel modeling algorithm is a crucial ingredient for fully automated pipelines, which is useful for many applications as shown above. However, identifying these structures remains a manual task (in this work), but

preparations (Sola et al. 2022) and efforts to develop automated detection methods using neural networks (e.g., Richards 2022; Domínguez Sánchez et al. 2023; Desmons et al. 2024) are an active field of research.

In Section 2 we present the data used in this work. All steps and the methods involved in producing the stream and tail models and measuring brightnesses are described in Section 3. Stellar streams originate from disrupted or disturbed galaxies. In the case of total disruption and absence of star formation, their total brightnesses conserved. Their color of the stellar population moves slightly to redder colors. From this consideration, we expect that streams that originate from dust-free passive galaxies remain on the red sequence. The validity of this statement and whether streams originate from passive galaxies or form a different class is addressed and discussed in Section 5. Tidal tails are only used to compare their colors to the streams and to test the modeling algorithm.

Throughout this work, we assume a flat cosmology with $H_0 = 69.6 \text{ km s}^{-1} \text{ Mpc}^{-1}$ and $\Omega_m = 0.286$ (Bennett et al. 2014). Luminosity distances and angular scales were calculated with the cosmological calculator by Wright (2006). All magnitudes are given in the AB system. When referring to a *feature*, the statement always includes both streams and tails. Otherwise, they are mentioned separately.

2. DATA

2.1. Telescopes and Surveys

2.1.1. 2.1 m Wendelstein Telescope

Primarily, the 170 g' band Abell galaxy cluster observations from Kluge (2020) are used in this work. All clusters fall into a redshift range of $z \lesssim 0.08$. Additionally, for the A1656 (Coma Cluster), r' -band data was available. The data was captured with the 2.1 m Fraunhofer Wendelstein telescope and its Wide Field Imager (WWFI; Kosyra et al. 2014), which encompasses four ev2 CCDs, each with $4096 \times 4096 \text{ } 15 \mu\text{m}$ pixels. Each detector has a field of view (FOV) of $13'.7 \times 13'.7$ and a pixel scale of $0''.2 \text{ pixel}^{-1}$. A total FOV of $27'.6 \times 29'.0$ for one exposure is achieved which includes the $98''$ north-south and the $22''$ east-west gap. By applying a dither pattern of 52 steps, the final observed field is increased up to $\sim 49'.3 \times 54'.0$.

2.1.2. Legacy Survey - DECaLS and BASS

To measure stream colors, we use existing WWFI r' band information for features in the Coma cluster. For all other features, we utilize Legacy Survey DR10 data in the g and r bands. The survey is split into several subsurveys from which our WWFI fields were covered by

the Beijing-Arizona Sky Survey (BASS) and the Dark Energy Camera Legacy Survey (DECaLS; Dey et al. (2019)). BASS uses the 2.3 m Bok telescope equipped with the 90Prime wide field imager. It consists of four thinned Lockheed 4096×4096 pixel CCDs and has an FOV of $1.16^\circ \times 1.16^\circ$ and a pixel scale of $0''.45 \text{ pixel}^{-1}$. DECaLS uses the 4 m Victor M. Blanco telescope. With 62 LBNL red-sensitive 2048×4096 pixel CCDs at the prime focus and a pixel scale of $0''.263/\text{pixel}$, it covers a field of 3 square degrees.

2.2. Data Processing

All data used was already reduced and coadded to final stacks. WWFI stacks were reduced with the WWFI data reduction pipeline (Kluge 2020; Kluge et al. 2020; Zöller et al. 2024). It was developed for brightest cluster galaxy (BCG) and intracluster light studies, which hence includes precise background subtraction with night-sky flats. Zero-points are calibrated to the Pan-STARRS DVO PV3 catalog (Flewelling et al. 2020) using apertures of $10''$ (50 pixels) diameter. Other effects such as additional offsets from the Pan-STARRS catalog, ghosts, and the missing light when increasing from $10''$ to $908''$ (infinity) apertures result in a zero-point correction of 0.1155 magnitudes for the g' -band, hence $ZP_{\text{inf}} = ZP_{50} + 0.1155 \text{ mag}$. When calculating g' band brightnesses of the tidal features, ZP_{inf} is used. However, for color analysis, ZP_{50} is needed because ZP_{inf} for the r' is not determined yet.

We use the final reduced data from the LS DR10, which are processed by the NOIRLab Community and Legacy Pipeline. Cutouts of the features were automatically obtained using the LS Sky Viewer. For all cutouts, we used a pixel scale of $0''.263 \text{ pixel}^{-1}$.

2.3. Data Inspection

The cluster stacks are manually inspected for signs of tidal features. We picked 15 features (nine streams and six tails), which have a high signal-to-noise ratio (S/N), show no sharp turns, i.e., a strong curvature, and are distinguishable from the merger/host. Further, these agree with the limitations of the modeling algorithm so we are sure that the modeling will succeed. We list those we found alongside their equatorial coordinates, that is the center of the feature, their redshift estimator, i.e., their host galaxy or cluster redshift, their angular scale, and their feature type in Table 1. All remaining tidal features, of any form, that were classified but not analyzed in this work are listed in Table 4 and Table 5. We note that for some features the classification is not straightforward and that it might not even be a tidal feature at all.

Table 1. List of selected tidal features (+1 Spiral Arm) Found in the WWFI Abell cluster sample. The redshift of the feature was estimated from its host, or if no host redshift was available, the redshift of the cluster.

α_{Feature} J2000 (1)	δ_{Feature} J2000 (2)	z_{Feature} (3)	z Candidate (4)	Angular Scale [kpc/''] (5)	Feature (6)
01:20:54.4	+19:30:58.6	0.0517070 (Bilicki et al. 2014)	LEDA 1595431	0.661	Stream
02:56:30.6	+15:55:22.8	0.0352480 (Lauer et al. 2014)	UGC 2413	0.706	Stream
10:24:32.5	+47:50:10.7	0.0600400 (Alam et al. 2015)	2MASX J10243254+4749361	1.167	Stream
10:25:14.3	+47:44:45.0	0.0621100 (Ahn et al. 2012)	NVSS J102511+474418	1.205	Stream
11:11:13.8	+28:44:04.4	0.0293400 (Ahn et al. 2012)	NVSS J111112+284243	0.591	Tail
12:59:26.6	+27:59:54.4	0.0239070 (Rines et al. 2016)	NGC4874	0.485	Stream
13:00:32.5	+28:02:01.8	0.0212000 (den Brok et al. 2011)	GMP 2617	0.432	Stream
13:01:04.2	+27:45:56.0	0.0276800 (Ahn et al. 2012)	LEDA 83751	0.559	Stream
15:11:55.2	+05:38:17.4	0.0514300 (Alam et al. 2015)	2MASX J15115519+0538171	1.010	Stream
22:49:59.6	+10:52:23.9	0.0787245 (Mahdavi & Geller 2004)	LEDA 1385552	1.491	Stream
23:12:43.8	+10:43:21.1	0.0221950 (Yu et al. 2022)	Mrk 526	0.451	Tail
23:12:41.7	+10:44:17.9	0.0221950 (Yu et al. 2022)	Mrk 526	0.451	Tail
23:13:29.9	+10:22:45.9	0.0649000 (Ledlow & Owen 1995)	z_{A2558}	1.255	Tail
23:13:27.6	+10:22:27.9	0.0649000 (Ledlow & Owen 1995)	z_{A2558}	1.255	Tail
(23:50:44.6	+27:16:41.7	0.0270370 (Yu et al. 2022)	MCG+04-56-014	0.546	Spiral Arm)

2.4. Data Preparation

We start with image cutouts either directly obtained from the LS sky viewer or created from the WWFI stacks. Typical sizes were $3'5 \times 3'5$. Then we assign the cutout, i.e., the feature, an identification key based on the abbreviation of tidal stream (TS) or tidal tail (TT) and the combination of the central coordinates of the feature (e.g., TS012054+193058 at R.A. $01^{\text{h}} : 20^{\text{m}} : 54^{\text{s}}$ and decl. $+19^{\circ} : 30' : 58''$). If a bright galaxy overlaps with the feature, an isophotal galaxy model is created (see Section 3.2) and subtracted from the stack. The remaining galaxies and stars are masked and stored in a source mask. Objects that are relatively large compared to the feature and significantly overlap with it are also masked but stored separately in an interpolation mask. In addition, a mask for every source in the image, including the feature, is created, which is used to create the error image (Section 3.6).

This set of images (e.g., Figure 1) for each feature is used for the modeling procedure and photometric measurements.

3. METHODS

3.1. Source Masking

Masks are created in a semiautomated procedure. First, sources are masked automatically based on the parameters that follow.

Threshold T_0

The threshold is either a signal-to-noise (S/N) or a surface brightness (SB) threshold. All pixels inside the detection area in the smoothed image with values above the threshold are masked.

expand diameter δ

All individual masks are expanded via a fast Fourier transform convolution with a circular kernel of a given size δ . Every masked pixel is replaced by this kernel, resulting in a more conservative mask.

border size s_{border}

All pixels which are s_{border} pixels away from the image border are set to zero, i.e., it performs an image crop. This is useful for wide-field images, where the S/N drops rapidly towards the border. In our case, it was always set to zero.

detection area a

A circular Gaussian kernel with a given standard deviation a represents the detection area. The background-subtracted image is convolved with it before the sources are detected. A larger parameter results in a higher masked pixel fraction while possibly missing smaller sources.

background box size s_{bg}

With the background box size, the image is divided into grid cells with the size of s_{bg} . In each cell, the pixel

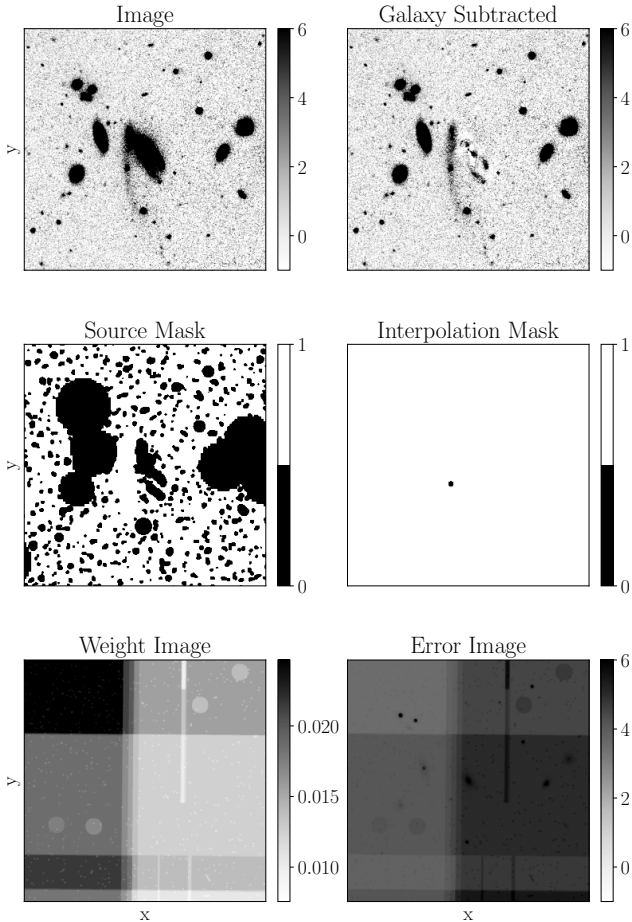


Figure 1. Set of images used for the modeling and photometric measurements. From left to right and top to bottom: (1) The reduced cutout. (2) Same as (1) but after the removal of the galaxy. (3) The source mask. (4) The interpolation mask. (5) The weight image cutout obtained from the data reduction. (6) The corresponding error image, which is determined by Equation 13.

values are $\kappa - \sigma$ clipped with a lower and upper limit of $\kappa = 3$ and $\kappa = 8$ respectively. After the clipping, the median of the remainder is taken as the background value in that cell. A spline interpolation through the grid is used to create a smoothed background model, which is subtracted from the image. It is also possible to subtract a constant. The constant is determined from all non-zero, non-Nan $\kappa - \sigma$ clipped pixel values, with a lower limit of $\kappa = 3$ and an upper limit of $\kappa = 4$.

The auto-mask is manually improved by unmasking the feature, expanding masks, and masking missed sources. We should emphasize that it is not necessary to mask every source in the image. Only contaminants near the feature have to be considered. However, for visual demonstration and model quality inspection, it is convenient to have a complete source mask.

3.2. Galaxy Subtraction

We subtract isophotal models of galaxies, which either have bright extended halos (large Es or BCGs) or cover a significant fraction of the feature. The models are created with a program that was developed for BCG modeling in Kluge (2020) and is based on PHOTUTILS (Bradley et al. 2023). The masks are created with the same method as described in Section 3.1. The ellipse fitting works as follows. First, infinitesimal ellipses are fitted to the inner isophotes, allowing for subpixel precision and averaging along their path. After that, the flux is remeasured from medium to large radii within elliptical rings. To remove statistical effects, i.e., outlier rejection, the median of those rings is taken instead of the mean. Ellipse parameters, such as semi-major axis radius, semi-minor axis radius, central coordinates, ellipticity, and position angle, are varied up to a fixed radius from which only the semiaxis radii are increased. Hence, it is important to note that the ellipses are fitted on changing radii, not on changing surface brightnesses. Both the inner and outer models are then combined into one full galaxy model.

From strong variations between the boxy and disk isophotes at very small radii, a butterfly/cross-shaped residual can occur. However, this effect is negligible, as only a small percentage of the model is affected, and for most of our sample, the feature does not reside near the center of its host. Still, if a residual arises and overlaps or interferes with the feature, we mask the corresponding region.

In some cases, more than one galaxy needs to be subtracted from the image. Here, we iteratively subtract the galaxies after one another and repeat the process to account for bright overlapping halos that cannot easily be masked. A similar approach is necessary if the feature is still connected to the galaxy. We begin with a first approximate galaxy model and subtract it. Then we improve the mask by having a much better vision of the feature’s position than before and create a second model afterward. This strategy improved the quality of the subtracted image significantly.

3.3. Feature Modeling

As a smaller satellite gets stripped and destroyed by a more massive host, it gets torn apart, leaving a stellar stream. In the absence of triggered star formation, this stream traces the characteristics of the progenitor galaxy, namely brightness, color, stellar mass, age, and metallicity. Even though triggered star formation could modify the stream’s stellar and gaseous properties from the progenitor galaxy, the faint component, i.e., the overall extent of the stream, should remain the

same. We define the bright component as concentrated and irregularly shaped regions of brighter flux, e.g., star formation clumps. A similar argument is posed onto tails and its ejected stellar material. Therefore, we use aperture photometry on the features where the aperture shape must be flexible due to the diverse morphologies. Manually drawing the aperture is time-consuming and not reproducible as the visibility of these LSB features strongly depends on how the flux is translated to a color map, e.g., for visual image inspection/analysis. To overcome this issue, we create a model of the feature via an analytic description of the brightness profile. This not only provides exact information about the feature but makes it possible to define a criterion for the shape, i.e., the width of the polygon aperture, in our case the FWHM. We describe our fitting procedure and define our empirically approximated functional form in the following Sections.

3.3.1. Scanner Algorithm

The algorithm is based on a simple idea: move a box along the feature and fit an analytic function to every box. The central 1D pixel slice perpendicular to the moving direction then represents the 1D pixel slice of the feature at the central x - and y -position of the box in the image. The algorithm is part of the author’s open source Python package `ASTROSTREAMPY`. It is available via PyPi or through GitHub, where a package wrapper is also provided to the user for quick usage. This Section does not explain the package or how to use it but focuses on an in-depth description of the algorithm and its principles.

First, we must assume that the image is prepared for the modeling as described in Section 2.4. Then, an initial box is placed manually on a region of the feature with a high S/N, preferably near the center. From there, the feature is scanned and modeled in both directions. In that way, the box reaches ever lower S/N regimes until the signal drops significantly below the background noise and an analytic function cannot be fitted anymore. Furthermore, the time it takes to finish the model is reduced, as both parts are done in parallel. With that, we maximize the fitted length of the feature. Otherwise, if we start the scanning at one end, most likely a low-S/N region, the fitting procedure could lose robustness and get trapped in a local minimum that badly represents the feature.

Furthermore, plausible box dimensions should be set. For example, if we assume the feature is purely vertical in the image, the width (i.e., the side perpendicular to the feature) should be large enough to cover enough background information. The box height (i.e., the side

length parallel) has similar constraints. A small box height could lead to a failure of the fitting as the scatter of the pixel values is too high, especially if the feature is only slightly above the local background. Vice versa, wider boxes increase the S/N, but they also lose information about the structure inside the feature. For a clearer understanding: one can imagine the box being averaged before fitting a Gaussian to it. Hence, a thicker box increases the S/N.

Before we continue with the details of the algorithm, we explain how a model is fitted in each box. The lower-left panel of Figure 2 shows a simulated stream segment in a box, which has, in this case, a width of 180 and a height of 30 pixels. The panel next to it is what we want to achieve, a clean residual image with only background noise left. The six smaller upper panels illustrate how the best fit is found. First, a distance grid (A) is created depending on the box dimensions, meaning the pixels in the central vertical slice have a value of zero, and all other pixels have a value regarding their x -distance to the center. We encourage the reader to see Appendix B for a detailed description of the construction of the distance grid.

With such a grid, we can produce a feature with a Gaussian profile perpendicular to its direction (B) by inserting the grid into $\exp(-\frac{x^2}{2})$. This Gaussian has an amplitude and standard deviation of 1 and is oriented vertically. Further, we rotate the grid, i.e., the Gaussian by an angle, and increase the amplitude (C). The angle is defined in a way that a positive value rotates counterclockwise. If the box is not centered on the feature, the grid needs to be offset concerning the central x - and y -position. An x -offset is performed, on the grid (D). With an increase of the standard deviation, we widen the stream (E). The last tuning is done by applying a skewness (F) and leaving us with a final stream model. This procedure is repeated for every slice. Of course, if necessary, we can vary the symmetric higher-order moments, i.e., h_2 and h_4 as well, which would introduce a kurtosis.

The parameter fitting for each box is done by the open source Python package `LMFIT-PY`. The `lmfit.Model` class takes a fit function as an argument and performs a least-squares minimization of the residuals. Apart from just returning to the routine and adjusting the fit parameters, we convolve the model by a Gaussian kernel with the size of the mean point spread function (PSF) across the image, which allows us to fit the intrinsic shape parameters of the stream. While the resulting model image represents the convolved version, the parameter table only contains the intrinsic best-fit values. With the selection of the initial box and its position, an

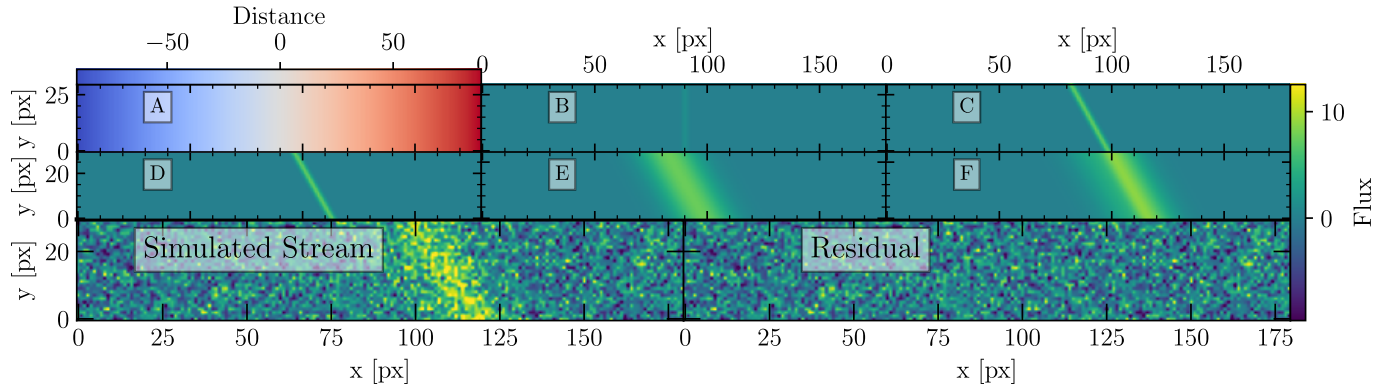


Figure 2. Illustration of the feature modeling. The flux mapping to a color map is identical for all panels except (A). (A) Distance pixel grid (see B). A 1 pixel distance corresponds to a value of 1 or -1 respectively. The color map is arbitrary and just for visualization purposes. (B) The distance grid fed into a Gaussian distribution with an amplitude and a standard deviation of 1. (C) The same Gaussian but with a rotated grid and with a higher amplitude. (D) The model position corrected by an x -offset. (E) The standard deviation increased. (F) Applied skewness. Note that the orientation and position parameters, i.e., α , x_0 , and y_0 are embedded in the grid before the Gaussian is applied.

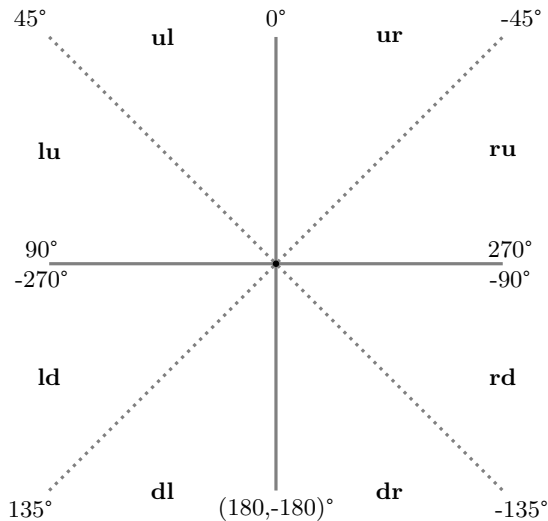


Figure 3. Schematic of the sectors, from which the algorithm determines its next box position. The definitions of the bold letters are: u -up, d -down, l -left, and r -right. The angles represent the angle of the stream increasing counter-clockwise. The point at the coordinate center resembles the center of the fitting box and each line follows the stream.

initial model is created. It is used as an "anchor" for both parts of the feature. The code is parallelized, such that both segments are modeled simultaneously using the previous best-fit parameters as initial guesses for the next box. To guarantee that the box remains centered on the stream at every iteration, the peak location of the Gaussian is compared to the center of the box. If there is a discrepancy, the current box center is corrected by either a x -, y - or x - y -offset. Based on that, we must tell the box where to move, as it has no global shape information of the feature. By defining a sector map (Fig. 3) with each sector spanning a 45° angle, we can

determine where to move the box based on the fitted grid angle. A keyword is assigned to the sector, e.g., if the feature angle is 78° , the value falls into the "lu" (left up) sector. Of course, "rd" would also be a true sector assignment, which would link to an angle of 258° or -102° . The naming is just the combination of the first letters of the primary and the secondary direction and is important for the modeling loop. At each iteration, the two possible sectors are compared to the prior. Based on that, the correct direction is used and translated to the true shift information. This method prohibits random direction flips of the box movement.

In cases where the stream curves beyond 45° the box dimensions flip, such that the shorter side remains parallel to the feature. Additionally, the width and height of the box change smoothly with the measured stream angle. This allows for a continuous transition from a vertical to a horizontal box, or vice versa. At the limit of 45° , the box becomes a square. The widths and heights are determined by two inverse tangent functions and are limited by the dimensions of the initial box. It needs to be noted that this approach slowly fails if the stream angle in the initial box deviates strongly from a purely horizontal or vertical feature segment. In the case of the sample used in this work, it was no issue, as the features remained almost straight. Hence, the use of dynamic box dimensions was turned off during the model creation.

As soon as the best-fit values are determined, a box model, i.e., the model of the current segment is created. The central 1D pixel slice of that model is then used as a model slice of the whole feature at that x - and y -coordinate. The slice used is always along the larger box side. With the step size being 1 pixel no gaps or overlaps are created, without considering a dimension

flip. To account for those cases, we take the average of the current model and the temporary model carrying the current 1D slice. Everything described up until now is repeated in each step of the modeling.

The LMFIT-PY library model fitting is designed to continue with previous parameters if no possible solution is found. To counter that behavior, we introduce termination thresholds:

- *Non-Gaussian Best Fit*: If consecutively (three times in a row) no peak in the model, i.e., no Gaussian fit, was found, the modeling terminates.
- *User Fixed Endpoints*: If the current box center is near (n pixel) one of the two endpoints, the modeling terminates after continuing for $2n$ steps.
- *S/N*: If the ratio of the fitted amplitude of the Gaussian and its fitting error is below a certain value, the modeling terminates.
- *Repeating parameters*: If the fitted amplitude of three successively fitted amplitudes is within a certain threshold, the modeling terminates.

If the endpoints are given, only the non-Gaussian threshold is checked; otherwise, we brute-force the modeling. This might introduce badly modeled end segments, but in general, those can be cut off later while inspecting the model quality and using the ASTROSTREAMPY built-in model modifier.

It should be noted that our approach with fixed boxes (i.e., their sides are always parallel to the image borders) might not be the best solution to the problem. It rather might be better to rotate the box and always keep it perpendicular to the feature. That would be a big improvement, as the dimensions stay the same, but additionally makes the problem more complex, as we cannot easily just take the central slice as a model anymore. While our approach is sufficient for features with a small curvature, the exact opposite poses a limit to our method. This is a limitation that might get updated in the future to also work for strong curved features.

3.3.2. Gaussian Fitting

In a first-order approximation, we use a Gaussian as the analytic fit function for every 1D slice of the feature. There might be a better solution, but we will show that our approach yields very promising results. However, for some features, a standard Gaussian is not sufficient, and they show substructure and altered shapes, possibly caused by star formation and gravitational forces acting upon the feature.

To account for these shape deviations, i.e., skewness (tilt) and curtosis ("tailedness") or combinations of both,

we use the Hermite basis functions. These functions are derived from a set of orthogonal polynomials, called the Hermite polynomials, and are defined as shown below.

$$H_n(x) = (-1)^n e^{x^2} \frac{d^n}{dx^n} e^{-x^2} \quad (1)$$

The order of the polynomial is given by $n \in \mathbb{N}$. Normalizing them by $1/\sqrt{2^n n!}$ and multiplying it with an amplitude parameter (h_n) we arrive at the Hermite basis functions.

$$H_2(x) = \frac{h_2}{\sqrt{8}} (4x^2 - 2) = \frac{h_2}{\sqrt{2}} (2x^2 - 1) \quad (2)$$

$$H_3(x) = \frac{h_3}{\sqrt{48}} (8x^3 - 12x) = \frac{h_3}{\sqrt{3}} (2x^3 - 3x) \quad (3)$$

$$H_4(x) = \frac{h_4}{\sqrt{384}} (16x^4 - 48x^2 + 12) \quad (4)$$

$$= \frac{h_4}{\sqrt{24}} (4x^4 - 12x^2 + 3) \quad (5)$$

In spite of that, the basis functions can create negative values in the model if the h_n deviates strongly from zero ($\gtrsim \pm 0.1$). To reduce this issue, we use a cumulative distribution function (CDF) instead of H_3 . We use the CDF from SCIPY (`scipy.stats.norm.cdf`), which is defined as

$$\text{CDF}(x, \sigma, s) = s \int_{-\infty}^x \frac{1}{\sqrt{2\pi\sigma^2}} e^{-\frac{(t-\mu)^2}{2\sigma^2}} dt, \quad (6)$$

where we add an additional amplitude parameter s , which should be equivalent to the h_n . The argument to use the CDF instead of the third Hermite basis function is that H_3 is most prone to fall below zero. Generally, negative values are allowed, as the local background should scatter around zero, but strong deviations are nonphysical for the light profile. Our final fit function is as follows:

$$F = A \left[e^{-\frac{1x^2}{2\sigma^2}} (1 + \text{CDF}(x, \sigma, s) + \sum_{i \in \{2,4\}} H_i(x/\sigma, h_i) \right] + b \quad (7)$$

We summarize all fit parameters of the modeling in Table 2.

3.4. Photometric Measurements

To measure fluxes of tidal features, a good aperture has to be chosen. However, the complex shape does not allow for a simple method, such as one circular aperture governed by a radius. Drawing a polygon by hand is one possibility, but leaves room for a large variation in shape. Not only does human accuracy vary, but it is also difficult to decide whether the polygon is too wide, too narrow, too long, or too short. In addition, manual processes are time-consuming, especially clicking on

Table 2. List of the Fit Parameters of the Gaussian Modeling. The first three rows are the fit parameters of the grid (see Appendix B). The rest are those of the analytic fit function (Equation 7).

Parameter	Description
α	Position angle of the feature inside the fitting box.
x_0	The x -offset of the center of the feature inside the fitting box.
y_0	The y -offset of the center of the feature inside the fitting box.
A	The global amplitude of the Gaussian.
σ	The standard deviation of the Gaussian.
b	The background offset of the Gaussian.
h_2	The amplitude of the second-order Hermite basis function (H_2).
s	The amplitude of the CDF resembling the third-order Hermite basis function (H_3).
h_4	The amplitude of the fourth-order Hermite basis function (H_4).

points to accurately follow a shape. A more robust and automated method is therefore required, especially to enable comparisons between same objects but different studies; a method that ensures that all feature pixels are within the aperture.

We use the best-fit parameters of each Gaussian (Equation 7) to calculate the FWHM for each slice along the feature. From now on, we use Γ_n as a symbol for the FWHM where n represents the multiples of the FWHM; e.g., Γ_3 would mean the flux inside three FWHM. From there, slice by slice, all pixels farther than half the Γ_n from the peak are set to zero. The other pixels are set to one. This is enough to create an aperture mask. Of course, the masking threshold can be adjusted to create wider or narrower apertures. In addition, we smooth the aperture by using a running mean along the Γ_n of all slices. The apertures are used to measure the key properties of the features, i.e., apparent and absolute magnitude, surface brightness, and width. We use Γ_1 for the central surface brightness and color, and Γ_3 for apparent and absolute magnitude.

Our goal is to create an aperture mask that encloses almost all of the feature’s flux. Therefore, we establish a 76–98–99.9 rule. For a standard Gaussian, within Γ_3 , $\sim 99.96\%$ of the distribution is covered (Appendix C). Even if the true percentage for higher-order Gaussians differs, it only adds values from the wings, which should scatter anyway around the mean local background, ideally zero. As such, we defined a robust way for feature apertures from Gaussian models.

There are cases in which galaxies or stars overlap with the feature. If the feature is broad enough and the sources are relatively small, those can be masked, and ASTROSTREAMPY will still be able to perform a good fit. Other scenarios involve either too many or too large sources and a relatively narrow feature. Both imply that too much area would be masked, and the fitting would fail in those regions. Those sources, which strongly overlap, are then interpolated with a 2D Gaussian Kernel

and a position angle ensuring that these pixels are interpolated along the stream. The position angle is important such that the interpolation happens along the aperture and allows for asymmetric kernels with different standard deviations for x and y . For photometric measurements, all pixels that were either used as a source mask or an interpolation mask are then filled with the corresponding information from the created model or remain zero. We rely on this approach, as measurements on the model and the true data differ on a $\sim 5\%$ level.

We measure the surface brightness as well as the apparent and absolute magnitudes for each tidal feature within an aperture that is based on the FWHM criterion. The flux inside the aperture is calculated via

$$F = \sum_{x=0}^n \sum_{y=0}^n (I_{xy} - \bar{\beta}) A_{xy} \quad (8)$$

where I_{xy} is the data pixel value, $\bar{\beta}$ the local background value, A_{xy} the pixel value of the aperture mask (image) with $A_{xy} \in \{0, 1\}$. Further,

$$m = -2.5 \log(F) + ZP \quad (9)$$

$$SB = -2.5 \log\left(\frac{F}{n \times \theta^2}\right) + ZP \quad (10)$$

holds, where θ is the pixel scale of the image in "pixel⁻¹ and n is the number of nonzero pixels inside the aperture given by $\sum_{x=0}^n \sum_{y=0}^n A_{xy}$. To obtain absolute magnitudes, we subtract the distance modulus $M = m - \mu$. Surface brightnesses are corrected for cosmological dimming via $F = (1 + z)^4 F$.

The local background is directly determined from the best-fit parameters. For each slice of the feature, we already have the information of the background level. We compute a weighted average of all offsets to obtain the mean local background $\bar{\beta}$. The quality of $\bar{\beta}$ then strongly depends on the number of available background pixels for each box. To some extent, the uncertainty of this

approach and the resulting background value are captured with a Monte Carlo Error Propagation (MCEP). We also encapsulate the mean background uncertainty in our flux error estimation using the standard error of the mean of all fitted offsets.

The effective surface brightness is measured at the effective radius. For that, we create another aperture, based on the model, where each pixel that is not at a distance of the effective radius from the center of feature, is set to zero. With this approach we get a 1 pixel wide border aperture, at which the surface brightness is measured.

3.5. Color Measurements

The BCG sample of Kluge et al. (2020) only covers the g' band. However, for some clusters, follow-up observations were performed for other studies, e.g., ultra-diffuse galaxy (UDG) populations in A262 and A1656 (Coma Cluster) in Zöller et al. (2024). The latter is for now the only cluster where the r' band of the sample is available. For all others, we utilize Legacy Survey DR10 data (LS-DR10 Dey et al. 2019). Eleven out of the 12 remaining features were covered by the LS-DR10 footprint. We extract cutouts and repeat the data preparation process for the LS r and g band. Further, feature models and photometric apertures are created with ASTROSTREAMPY. We compare each image, model, residual, and aperture in every filter to decide which aperture is best for the color measurements. The strongest criteria here are the quality of the aperture mask and how well it traces the shape of the stream and does not show any artifacts from the creation process, i.e., missing parts or unwanted shapes.

Before we apply the final selected aperture, we discard every pixel that was either masked or interpolated (see Section 2.4) in every band. In that way, we ensure that first, only the same pixels are measured, and that we only measure the true color of the feature. Similar to color measurements of stars, we do not use the complete feature, as we assume that the color measurement is most reliable in the inner regions, i.e., inside one FWHM. Further for the WWFI colors, we use the ZP_{50} , instead of ZP_{inf} , and the standard ZP of the Legacy Survey of 22.5 mag.

The colors are used to transform measured g' brightness into the V band following Jester et al. (2005), which is necessary for comparisons with various galaxy types in the $M_{\text{tot}} - r_e$, $\mu_e - r_e$ and $M_{\text{tot}} - \mu_e$ parameter spaces. We have to compensate for discrepancies between the WWFI g' (Pan-STARRS) and the Sloan Digital Sky Survey (SDSS) g band via $g = g' + 0.08$ and $r = r' + 0.01$ for the Sun (see Tonry et al. 2012; Willmer 2018). This

results in Equations 11 and 12, which transforms g' into V depending on the used color. The total absolute V band magnitudes are further utilized to calculate the luminosity of the features in units of solar luminosities via $L = 10^{0.4(M_{V,\odot} - M_V)} L_\odot$, where $M_{V,\odot} = 4.80$ is the solar absolute V band magnitude from (Willmer 2018).

$$V_{\text{WWFI}} = g' - 0.59(g' - r') + 0.0287 \quad (11)$$

$$V_{\text{LS}} = g' - 0.59(g - r) + 0.07 \quad (12)$$

Additionally, for comparisons with cluster members in the Coma cluster, we apply a correction of the distance modulus and subtract a K correction term from the total absolute magnitude. In this manner, the measured brightnesses are converted into one rest frame. All K terms were determined with a calculator (Chilingarian & Zolotukhin 2012).

3.6. Error Evaluation

3.6.1. Modeling Uncertainties

Final brightnesses mainly depend on the quality of the model and its Γ_n aperture. Hence, we estimate additional uncertainties introduced by the modeling algorithm. Covariance matrices are directly provided by the used least-square-minimization package and utilized to perform an MCEP to quantify the impact of the best-fit parameters on the size and shape of the aperture mask. One stream model is created to obtain a sample of best-fit parameters for each slice. Then, 25 times for each slice of the feature, a new best-fit parameter set (bottom half of Table 2) is drawn from a multivariate distribution governed by the covariance matrix. From there, we have 25 slightly different apertures, measure the magnitudes, and take the standard deviation of all results as an error representing an aperture error. This procedure was performed for two different streams from Table 1, one simple (TS012054+193028) and one complex (TS125926+275954), with higher-order terms enabled. For both, the 25 measurements for slightly different apertures scatter within a standard deviation of 0.005 magnitudes.

Not only do the fit parameters themselves hold an uncertainty, but the modeling depends on where the initial box placed and what its dimensions are. This robustness was captured by creating 50 models of the same feature with different initial boxes. The first box was set manually. Then, its width, height, and position were randomly varied within a certain range. For every model, an aperture was created, and the corresponding apparent magnitude and surface brightness were measured. The standard deviation of these measurements represents the robustness of the algorithm (Section 4.2). For the total brightness, we find a scatter

of $\Delta m_\sigma = 0.009$ mag and for the surface brightness, a value of $\Delta SB_\sigma = 0.013$ mag arcsec $^{-2}$.

3.6.2. Photometric Uncertainties

Flux errors inside the apertures are calculated from error images that contain the flux uncertainty for every pixel. We follow a method to generate error stacks from the stacked science images, which is described in detail in Zöller et al. (2024). The flux uncertainty in a pixel at positions x and y can be approximated by

$$E(x, y) = \left\{ \frac{|\mathcal{D}(x, y)| \times \text{median}\{\mathcal{W}\}}{\mathcal{G} \times \mathcal{W}(x, y)} + \left(\frac{\text{std}\{\mathcal{D}_m \times \sqrt{\mathcal{W}_m / \max\{\mathcal{W}\}}\}}{\sqrt{\mathcal{W}(x, y) / \max\{\mathcal{W}\}}} \right)^2 \right\}^{1/2}, \quad (13)$$

where \mathcal{D} is the image, \mathcal{G} is the gain of the camera, \mathcal{W} is the weight image, \mathcal{D}_m is the masked image, and \mathcal{W}_m is the masked weight image. For the WWFI stacks, weight images are a byproduct of the data reduction and store information on the spatially varying depth and, consequently, spatially varying S/N. For the Legacy Survey, we assume a constant weight over the entire FOV. The error flux inside the feature apertures is measured and added/subtracted to the feature's flux and translated into brightness errors.

$$\Delta F = \sum_{i=0}^n \sum_{j=0}^n E_{ij} A_{ij} \quad (14)$$

$$\Delta SB^\pm = \Delta m^\pm = \Delta M^\pm = -2.5 \log \left(\frac{F \mp \Delta F \mp \Delta \beta}{F} \right) \quad (15)$$

Here, $\Delta \beta$ is the cumulative background uncertainty of the local background estimated from the standard error of the mean of all Gaussian offset errors of every model slice, multiplied by the number of pixels inside the aperture. Note that the uncertainties for the surface brightness and total magnitudes still differ because the surface brightness flux is dimmed by the mentioned factor.

We overestimate the global brightness errors by adding the modeling uncertainties to the photometric error. This error is propagated to the color error via

$$\Delta(g' - r') = \sqrt{\Delta g'^2 + \Delta r'^2}. \quad (16)$$

The uncertainty of the width of the stream, both the Γ_1 width w and the effective radius r_{eff} , depend on the integer-based construction of the corresponding apertures and from which the widths are calculated, and the

scatter of the mean widths of the apertures created via the MCEP. Both add up to a width error of $\Delta w = 2$ pixels, where we assumed the MCEP error to be consistent for all features.

4. MODELING PERFORMANCE

4.1. Model Quality

In addition to visual confirmation of a successful model from either the residual image or a slice inspection, we quantify the fit quality by the ratio of the modeled and measured flux. If we compute the ratio of the measured fluxes on the real image and the created model within the same aperture, we are able to extract how precise we get in our (small) sample. Figure 4 shows four histograms, one for the surface brightness SB , the total absolute magnitude M_{tot} , the surface brightness inside the effective radius $\langle SB_e \rangle$, and the surface brightness at the effective radius SB_e . The mean surface brightness inside an aperture is less prone to outliers, i.e., noise peaks or other effects. We reach an accuracy of $\approx 3\%$ in $\langle SB_e \rangle$. Otherwise, M_{tot} and SB_e are affected strongly, especially the latter, which is an annulus with a width of just 1 pixel. Hence, the accuracy is smaller with $\sigma \approx 9\%$. Analogous to that, we constraint the model quality with respect to the width of the feature. We utilize the best-fit parameters of the model (true) of TS012054+193028 and its injection (model), which was the model with added noise and remodeled by `astrostreampy` and investigate the Gaussian standard deviation σ_G fit parameter (see Figure 5). The ratio of the true and model width profile, i.e., σ_G as a function of the slice position, is computed, and its average represents the mean precision of the mean stream width along its full extent, which is $\overline{\sigma_G} = \sigma_G^{\text{true}} / \sigma_G^{\text{model}} \approx 3\%$.

4.2. Influence of the Initial Box

We create 50 models of the stream TS012054+193028 with different initial boxes. The central coordinates, width, and height are changed randomly by a few pixels. We set the maximum number of model iterations to 200 to ensure that the full extent of the stream is captured, without reaching regions with low S/N that are prone to result in erroneous models. For each of the 50 models, we create Γ_1 apertures and measure the surface brightness and compute the corresponding flux uncertainty. We show the result in Figure 6. Additionally, we compute the median ($SB \approx 25.3713$ mag arcsec $^{-2}$) and standard deviation ($\Delta SB \approx 0.0474$ mag arcsec $^{-2}$) of the 50 measurements and plot it as a 1σ horizontal error stripe. Six outliers show brighter values, which are caused by earlier modeling terminations of the lower/fainter part of the stream. Hence, the surface brightness inside the

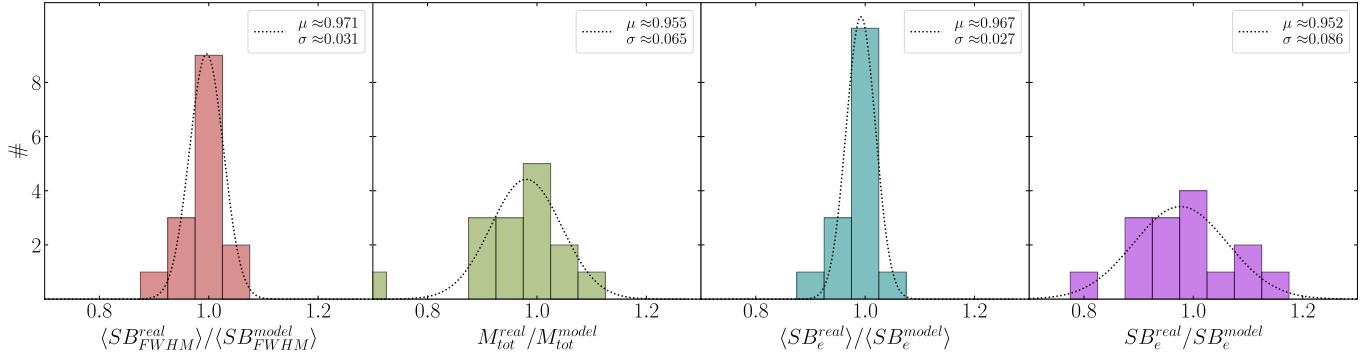


Figure 4. Histograms of the flux ratios of the feature measurements on the real data and the created model. The dotted line represents the fitted normal distribution to each measurement with the corresponding mean μ and standard deviation σ displayed in the legend. Note that we subtract the fluxes and not divide magnitudes. The x -axis label is a convenience for the reader.

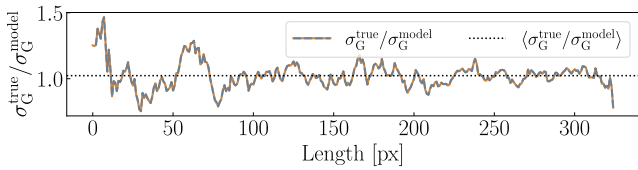


Figure 5. Ratio of the best-fit standard deviations of the Gaussian slices along TS012054+193028 of the real feature and the injected model. The mean ratio of ~ 1.02 is given by the dotted line.

aperture is brighter. We emphasize that this analysis is performed without checking the models, making it a blind check of the robustness. If we discard these six points, the standard deviation reduces to $\sigma \approx 0.013$ mag arcsec $^{-2}$. We see that the scatter of the surface brightnesses is comparable to the measured flux uncertainty. The same can be applied to the total brightness, which results in a clipped scatter of ~ 0.009 mag. Both values are added to cumulative brightness errors.

4.3. Injection Recovery Test

Gaussian noise is introduced to one of our feature models (truth) and used to remodel it with the algorithm. We compare the best-fit parameters and fit uncertainties of both models. A comprehensive analysis for the amplitude parameter A is presented in Figure 7. We show the truth in orange and three injections with different orientation angles, i.e., $\alpha \in \{0^\circ, 45^\circ, 90^\circ\}$. In all scenarios, we manage to retrieve the best-fit parameters for the amplitude profile within a 2σ interval from the original model. The x -axis is denoted as “length”, and corresponds to the pixel information on the image, specifically, the centers of the boxes along the feature. In this context, the y box centers align with the vertically oriented stream, while all other orientations are mapped onto the same coordinate system.

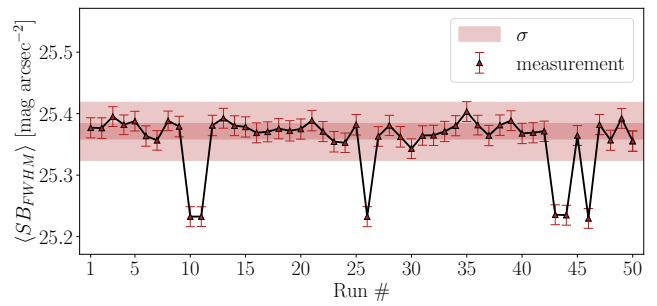


Figure 6. Surface brightness robustness of 50 TS012054+193028 stream models. Measurements are shown in black triangles with corresponding brightness error bars in red. Two 1σ error stripes are overlaid, of which the more opaque one is the standard deviation of all data points and the less opaque without the outliers. Note that the error bars of the surface brightnesses are only coming from the flux error image and are not the same errors computed for the final results.

5. RESULTS

5.1. Stream and Tail Catalog

One objective of this study is to compile a catalog detailing the structural characteristics of stellar tidal streams. While a listing of stream features around nearby galaxies exists in the SSLS (Martínez-Delgado et al. 2023a) and in Miró-Carretero et al. (2023), those only encompass surface brightnesses and colors. We build a catalog of different streams up to $z \sim 0.08$ and incorporate additional physical properties, which are not present in the mentioned literature catalogs. Additionally, in this work we add tails for a more comprehensive overview.

Although the number of features examined in this study is manageable, the total number of detected features is anticipated to rise significantly with forthcoming deep surveys due to their increased depth. Therefore, establishing a standardized naming convention is imper-

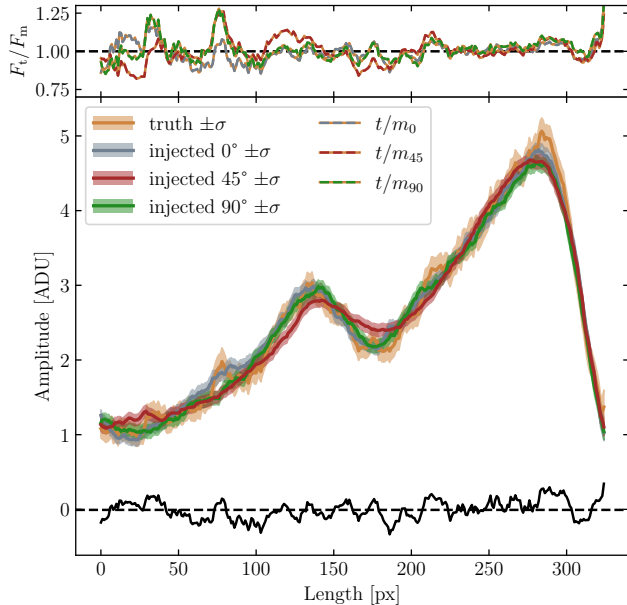


Figure 7. Fitted amplitude parameters of four TS012054+193028 models. Brown represents the model obtained from the original image. Gray is the same model injected into Gaussian noise. The same was done for green and red, but the model was rotated by 90 and 45° respectively. The residual from the model and the injected 0° model is shown in black. The mean of this residual is displayed by the black dashed line. The ratios of the flux profiles of the 0° to the 45° and 90° model are shown in the top panel. Here, the black dashed line shows a constant ratio of 1.

ative to ensure clarity and distinction. One proposed naming convention involves employing a general abbreviation followed by the R.A. and decl. coordinates. For stellar tidal streams, we advocate the format outlined below, as already adapted throughout this work.

We provide an example for the stream TS012054+193028. Here, ‘012054’ represents the R.A. of 1^h, 20^m, and 54^s, while ‘+193028’ signifies the decl. of +19°, 30′, and 28″. The feature coordinates are chosen to be the center of it, i.e., the point halfway along the feature. Note that for fully/multiple looped streams, this is not straightforward anymore. Here, one could choose either any point on the feature or its centroid. The prefixes ‘TS’ and ‘TT’ denote “Tidal Stream” and “Tidal Tidal”, respectively.

Following the steps described in Section 3, we present the feature properties in our WWFI stream and tail catalog in Table 3. Direct comparison to the stream sample in the SSLS (Martínez-Delgado et al. 2023a) is not possible because there is no overlap with the WWFI cluster survey (Kluge 2020). However, we can generally compare the measured g' -band surface brightnesses and ($g' - r'$) colors. We measure mean stream surface bright-

nesses of $\sim 26.25 g' \text{ mag arcsec}^{-2}$, which is brighter than the average $\sim 26.9 g \text{ mag arcsec}^{-2}$ from the SSLS. This is most likely caused by our different choice of where we measure the surface brightness. We average the surface flux in the central Γ_1 region, whereas circular apertures along the stream are used in the SSLS, which includes the full area.

In addition, we compute mean detection depths following Román et al. (2020):

$$\epsilon = -2.5 \log \left(3 \frac{\text{std}\{\mathcal{D}_m\}}{7'' \times \theta} \right) + \text{ZP} \quad (17)$$

where \mathcal{D}_m is the masked image, θ the pixel size of the image in arcseconds and the $7''$ comes from the typical size of the features in this sample. It computes the surface brightness that results for a flux level of three times the standard deviation of the background for the given area. The SSLS is deeper $\epsilon_{\text{SSLS}} = 28.89 \text{ mag arcsec}^{-2}$ than our sample $\epsilon_{\text{WWFI}} = 28.38 \text{ mag arcsec}^{-2}$. Hence, we attribute the larger fluxes in our work to selection effects. Regarding ($g' - r'$) colors, our results are consistent with the streams in the SSLS, namely all share similar values, ranging from 0.49 – 0.96 (SSLS) and 0.45 – 0.90 (this work).

We note that these measurements are also slightly affected by the choice of the redshift of the feature. As we do not have photometric or spectroscopic redshifts of the features directly, we assumed either the cluster redshift or that of the most probable host galaxy.

5.2. Structural Parameters

In Figure 8, the structural parameters, i.e., effective radius R_e , effective surface brightness μ_e and the total V -band brightness M_{tot} , of eight out of the nine streams in our sample (TS025630+155522 had no complementing r' -band) are investigated. For reference, we show other various types of galaxies. The original figure is Figure 37 in Kormendy et al. (2009). It was further updated by Kormendy & Bender (2012), Bender et al. (2015), and Kluge et al. (2020). Green points show the structural parameters for Ellipticals from Bender et al. (1992) and Kormendy et al. (2009) as well as classical bulges from Fisher & Drory (2008), Kormendy et al. (2009), and Kormendy & Bender (2012). The orange data points are BCGs from Kluge et al. (2020) who used the same imaging dataset as in this work. Local group spheroidals are from Mateo (1998), and McConnachie & Irwin (2006) and Virgo spheroidals from Ferrarese et al. (2006), Kormendy et al. (2009), and Gavazzi et al. (2005), both shown in light gray. A catalog of newer local dwarfs, summarized in a database (Pace 2024), is shown in slate gray. They help to populate the faint

Table 3. List of 14 tidal features (+1 Spiral Arm) and Their properties detected in the 170 Wide Field Abell cluster observations with the Wendelstein Telescope. Column (1) gives the suggested general name of the feature. Column (2) shows the g' band surface brightnesses inside Γ_1 . Columns (3) and (4) show absolute g' and V -band magnitudes. (5) ($g' - r'$) color. Column (6) shows Solar luminosities. Columns (7) and (8) show the effective g' -band surface brightness at the effective radius. Columns (9-10) show the shape properties' length and width.

Stream	SB_{FWHM} (g' mag arcsec $^{-2}$)	M_{tot} (g' mag)	M_{tot} (V mag)	($g' - r'$) (mag)	L ($10^9 L_{\odot}$)	μ^{eff} (V mag arcsec $^{-2}$)	r^{eff} (kpc)	w (kpc)	l (kpc)
(1)	(2)	(3)	(4)	(5)	(6)	(7)	(8)	(9)	(10)
TS102432+475010	26.949 \pm 0.026	-14.97 \pm 0.04	-15.2 $^{+1.0}_{-0.5}$	0.5 $^{+1.6}_{-0.8}$	0.1 \pm 0.06	27.017 \pm 0.026	1.2 \pm 0.5	3.0 \pm 0.5	33.5 \pm 1.7
TS102514+474445	26.632 $^{+0.026}_{-0.025}$	-16.88 \pm 0.04	-17.4 $^{+0.4}_{-0.3}$	0.9 $^{+0.7}_{-0.5}$	0.74 $^{+0.22}_{-0.21}$	26.578 \pm 0.025	2.9 \pm 0.5	8.4 \pm 0.5	49.8 \pm 1.7
TT111113+284404	24.848 \pm 0.019	-18.075 \pm 0.016	-18.31 $^{+0.08}_{-0.07}$	0.52 \pm 0.12	1.75 \pm 0.12	25.056 \pm 0.019	1.97 \pm 0.24	4.38 \pm 0.24	44.8 \pm 0.9
TS125926+275954	26.374 \pm 0.023	-18.486 $^{+0.026}_{-0.025}$	-18.85 \pm 0.04	0.67 \pm 0.04	2.89 \pm 0.09	26.452 \pm 0.023	5.06 \pm 0.2	15.91 \pm 0.2	95.9 \pm 0.7
TS130032+280201	27.049 \pm 0.023	-14.872 $^{+0.028}_{-0.027}$	-15.32 \pm 0.04	0.8 \pm 0.05	0.111 \pm 0.004	27.061 \pm 0.023	1.83 \pm 0.18	5.44 \pm 0.18	24.5 \pm 0.7
TS130104+274556	26.601 \pm 0.021	-16.872 \pm 0.021	-17.14 \pm 0.04	0.5 \pm 0.06	0.596 $^{+0.021}_{-0.022}$	26.648 \pm 0.021	4.17 \pm 0.23	12.41 \pm 0.23	37.8 \pm 0.8
TS012054+193028	25.256 \pm 0.022	-18.32 \pm 0.024	-18.72 $^{+0.12}_{-0.11}$	0.79 $^{+0.2}_{-0.18}$	2.55 $^{+0.26}_{-0.27}$	25.189 \pm 0.022	2.2 \pm 0.5	6.7 \pm 0.5	69.4 \pm 1.5
TS151155+053817	26.469 \pm 0.021	-17.453 \pm 0.021	-17.88 $^{+0.15}_{-0.13}$	0.84 $^{+0.24}_{-0.21}$	1.18 \pm 0.15	26.784 \pm 0.022	3.1 \pm 0.5	9.1 \pm 0.5	79.2 \pm 1.5
TS224959+105223	25.264 \pm 0.022	-18.742 \pm 0.025	-19.04 $^{+0.13}_{-0.11}$	0.63 $^{+0.2}_{-0.18}$	3.4 \pm 0.4	25.324 \pm 0.022	4.0 \pm 0.6	11.7 \pm 0.6	59.9 \pm 2.1
TT231243+104321	25.22 \pm 0.04	-15.36 $^{+0.06}_{-0.05}$	-15.5 $^{+0.17}_{-0.15}$	0.35 $^{+0.28}_{-0.24}$	0.131 $^{+0.019}_{-0.02}$	25.18 \pm 0.04	0.78 \pm 0.19	2.26 \pm 0.19	12.4 \pm 0.7
TT231241+104417	23.857 \pm 0.022	-17.194 \pm 0.023	-17.44 \pm 0.08	0.54 $^{+0.13}_{-0.12}$	0.79 \pm 0.06	23.864 \pm 0.022	0.98 \pm 0.19	2.62 \pm 0.19	15.8 \pm 0.7
TT231329+102245	25.852 \pm 0.025	-16.74 \pm 0.04	-17.14 $^{+0.27}_{-0.21}$	0.8 $^{+0.5}_{-0.4}$	0.6 \pm 0.13	26.056 \pm 0.026	2.9 \pm 0.6	8.3 \pm 0.6	20.8 \pm 1.8
TT231327+102227	25.362 \pm 0.022	-17.683 \pm 0.024	-18.02 $^{+0.16}_{-0.14}$	0.7 $^{+0.27}_{-0.24}$	1.35 \pm 0.19	25.162 \pm 0.021	2.4 \pm 0.6	7.8 \pm 0.6	35.9 \pm 1.8
SA235044+271641	25.674 \pm 0.022	-16.751 \pm 0.024	-16.95 $^{+0.11}_{-0.1}$	0.45 $^{+0.18}_{-0.16}$	0.5 \pm 0.05	25.553 \pm 0.022	1.82 \pm 0.22	5.57 \pm 0.22	31.4 \pm 0.8
TS025630+155522	25.636 \pm 0.02	-17.166 \pm 0.017	-	-	-	-	1.38 \pm 0.29	3.81 \pm 0.29	40.8 \pm 1.0

regions. The A1656 UDG sample (blue squares) is from Zöller et al. (2024). Disks are grouped into dwarf disks (Pildis et al. 1997; Makarova, L. 1999; Kirby et al. 2008), S0 disks (Baggett et al. 1998; Gavazzi et al. 2000; Laurikainen et al. 2010; Kormendy & Bender 2012), and normal disks (Baggett et al. 1998; Gavazzi et al. 2000; Ferrarese et al. 2006; Laurikainen et al. 2010; Kormendy & Bender 2012). A detailed figure of the disks can be found in Kormendy & Bender (2012). Red diamonds with a black outline display the stellar tidal streams studied in this work. While they are extended elongated objects, the classical definition of R_e does not hold. We measure the effective width along the minor axis, whereas the definition of R_e is along the major axis of an ellipse. However, we assume that when a satellite gets accreted, the effective radius does either not change or increase over time and is consistent with the effective width of the stream, i.e., the width of a Gaussian, within half of the total flux is captured. Furthermore, we must modify the effective width, since it is uncertain whether our measured effective width equates to the semi-major axis effective radius. A galaxy is also statistically unlikely to get stripped exactly parallel to its major or minor axes. Therefore, we assume that the measured effective width corresponds to the mean radius of an ellipse. Thus, we use $R_e^{\text{major}} = R_e / \sqrt{b/a}$, where R_e is the effective radius and R_e^{major} is the corrected effective width. We take the mean axis ratio of $b/a = 0.76$ from the Coma cluster members in Zöller et al. (2024), which is consis-

tent with the expected distribution of spheroid-shaped galaxies (Ryden 1996; Padilla & Strauss 2008).

The faint and elongated streams overlap with the UDGs in Figure 8 (top panel). However, the streams are brighter by a few magnitudes in total brightness M_{tot} (bottom panel). A similar trend is observed in the $M_{\text{tot}} - R_{\text{tot}}$ parameter space, where they shift toward the brighter end of the spheroidal population, predominantly aligning with S0 and normal disks.

5.3. Coma Red Sequence

Another tool to study the nature of streams involves examining whether they align with the red sequence of galaxies (Figure 9). This might give an additional insight into what type of progenitor galaxy was stripped. Passive galaxies follow a red sequence because the optical colors barely evolve after an age of 9 Gyr (e.g., Bruzual & Charlot 2003). The tilt can be explained by the mass-metallicity relation (e.g., Gu et al. 2020). In scenarios where star formation is absent, often in dry minor mergers, the colors and total luminosity remain unchanged. Therefore, the properties of streams, which may originate from early-type galaxies (ETGs), are expected to align with the red sequence. To achieve this, we utilize the red sequence data of the Coma cluster (Zöller et al. 2024) and compute rest-frame colors by applying K corrections and correcting the total brightnesses with the distance modulus.

The result is shown in Figure 9. In the upper panel, both streams (in red) and tails (in blue) are plotted in

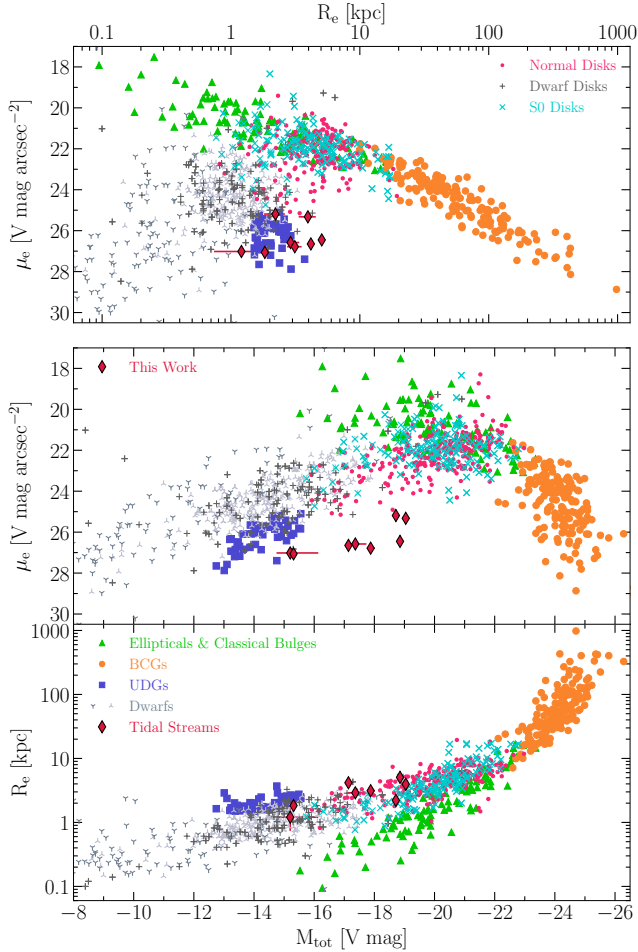


Figure 8. $R_e - \mu_e$, $M_{\text{tot}} - \mu_e$ and $M_{\text{tot}} - R_e$ parameter spaces of the tidal streams (red diamonds) in this work compared to dwarfs (light gray and slate gray)

, UDGs (blue), ellipticals (green), BCGs (orange), dwarf disks (dark gray), S0 disks (cyan), and normal disks (magenta). Kormendy et al. (2009) delivered the basis for this figure with updates in Kormendy & Bender (2012), Bender et al. (2015), and Kluge et al. (2020).

the color-magnitude space. Both distributions occupy the brighter end, albeit exhibiting considerable dispersion around the narrow limits of the red sequence, due to the high measurement uncertainties. The middle panel focuses solely on the streams within our sample. The error bars are the same as in the top panel but not shown, as only the positions of the streams on the red sequence matter here. On the whole, streams align with the red sequence within 2σ .

The bottom panel highlights the three streams within the Coma cluster. While those located outside the cluster are calibrated solely to the Coma distance, we scrutinize their positioning on the red sequence. The largest stream TS125926+275954 demonstrates good

agreement with the red sequence, which is unsurprising given its relatively large apparent size, and luminosity, and visual color. Similarly, tails are also located at the bright end of the red sequence within a 1σ confidence. They, however, show a slight trend toward bluer colors than the streams do.

6. DISCUSSION

6.1. Progenitors of Streams

We undertake a comparative analysis of the structural parameters of tidal streams against those of ellipticals, BCGs, spheroidals, disks, and UDGs to elucidate their positioning within the depicted parameter spaces (Figure 8). This comparison is needed to infer possible progenitor candidates for the streams in our sample.

There are three main properties we want to consider in this discussion: (1) The total brightness, (2) the color (also see Section 6.3), and (3) the size, i.e., effective radius (also see Section 6.2). Those strongly depend on the age of the stream, i.e., the time passed since the first stripping of stars. The total brightness further depends on star formation in the stream. If star formation is triggered by the tidal forces, bright massive stars form, and this would increase the total brightness of the stream, even long after their formation. **The color would not be strongly affected if the stream is older than 1 Gyr (Bruzual & Charlot 2003), as those stars quickly move to the red giant or supergiant branch.** In addition, the stream gets redder due to the aging of its stellar population, i.e., the population of its progenitor.

Beforehand, we split our stream sample into three categories based on the definition of dwarf galaxies as they are most commonly associated as tidal stream progenitors. The dwarf regime is generally defined as fainter than $M_V = -17$ mag (e.g., Tammann 1994) or sometimes with a more conservative approach of $M_V \gtrsim -18$ (e.g. Grebel et al. 2003). It follows that we have two faint streams (TS102432+475010, TS130032+280201), with M_V fainter than -17 mag, three "standard" streams (TS102514+474445, TS130104+274556, TS151155+053817), with $-18 \leq M_V \leq -17$ and three bright streams (TS012054+193028, TS224959+105223, TS125926+275954) with $M_V \leq -18$.

BCGs

Generally, BCGs are ruled out as progenitors. Given their status as the brightest and most-massive galaxies in the Universe, any interaction involving a BCG as the infalling less-massive merger member would still result in a major merger rather than a tidal stripping event.

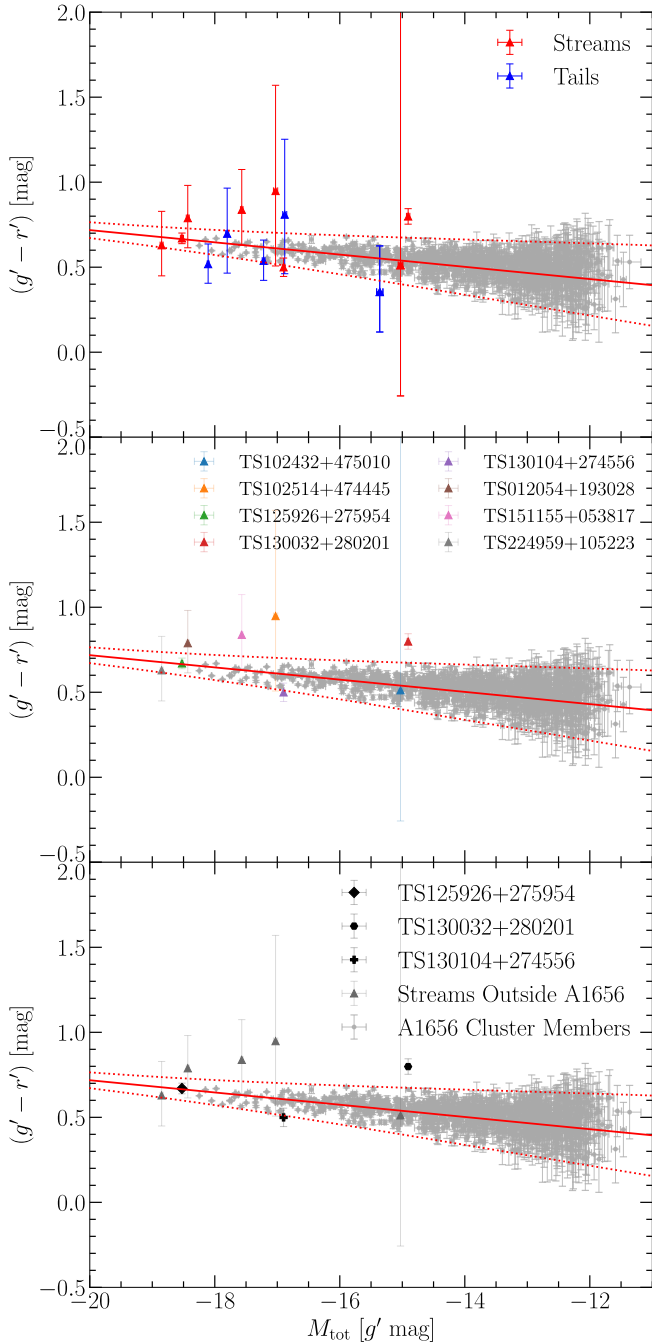


Figure 9. Tidal streams and tails compared to quiescent cluster member galaxies in the Coma cluster. Gray points with error bars are from the analysis in Zöller et al. (2024). Streams are shown in red, and tails are shown in blue with corresponding error bars. Only tidal streams in triangles with corresponding names are plotted in the middle panel. Highlighted streams originally located in the Coma cluster with diamond, hexagonal, and cross-shaped markers are plotted in the lower panel. Triangles are the remaining streams.

Therefore, BCGs are generally not considered as plausible progenitors for tidal streams.

Dwarfs

To reach the luminosity of our bright streams, progenitors from the dwarf population need to increase their flux by up to a factor of 2.5, even when using the conservative definition of $M_{V, \text{Dwarf}} \geq -18$. For those, a dwarf progenitor is unlikely, whereas for the faint and standard streams, dwarfs are a valid progenitor candidate. We justify this claim, as the bright streams are still connected to their progenitor. As a lot of flux is still present in the progenitor nucleus, the true total brightness would increase significantly. Additionally, we observe them early in their formation, which would mean that it is likely that newborn stars make them bluer. However, we observe red colors, namely 0.79, 0.63, and 0.67, respectively. We conclude both arguments make a (conservative) dwarf even more unlikely. For the large stream in the Coma cluster, i.e., TS125926+275954, it is also possible that the stream has two progenitors, due to its strong asymmetric shape and two overlapping galaxies with similar width.

For the faint streams, dwarfs are the only possible explanation, because they are fainter than the faint end of the disk, S0 and E population. Also, the size arguments holds, as the faint streams populate the bright-large end of the dwarf population.

A dwarf progenitor example from the literature comes from Foster et al. (2014), who studied the stream around the Umbrella galaxy, NGC 4651, and measured a total brightness of $M_V = -17.0$, which is consistent with that of dwarf galaxies. They further assume an effective radius of $R_e \sim 1 \text{ kpc}$ and label the progenitor as a dwarf elliptical. This measurement agrees well with our stream sample in the bottom panel of Figure 8.

Disks, Ellipticals, or S0s

We further investigate S0 and normal disks, as well as ellipticals as other potential progenitors. Among the bright streams, S0 or ellipticals are favored due to their gas loss and low to negligible star formation rates, consistent with the observed red colors of the streams (see 9). Distinguishing from S0s or Es as progenitors is difficult due to the behavior of the effective width of the stream. If R_e would increase, the stream moves upward in the lower panel of Figure 8, which would explain their origin from ETGs. The other scenario involves a non-changing R_e and hence would suggest S0 progenitors. This leaves both as plausible candidates for the origins of these three streams. A study by Errani et al. (2015) shows increasing width, but this depends on the time

at which we observe the stream. Therefore, we cannot claim either S0 or ETGs progenitors.

We apply the same arguments for the standard streams, as they show similar brightnesses as the faint end of the disk, S0 and E population. The difference is that for those, dwarfs can also be considered.

Both the $M_{\text{tot}} - \mu_e$ and $R_e - \mu_e$ parameter spaces have the same implication. Streams move downward in the middle panel of Figure 8 because their area increases simply from tearing apart the progenitor galaxy while the flux is conserved. Lastly, the upper panel shows both arguments for μ_e and R_e . Namely, with an increased area and constant brightness, the surface brightness decreases. Again, we cannot imply any evolution of R_e in this panel. Both arguments are also valid if the brightness would increase due to star formation. The descent is then diagonal, but still does not exclude any of the progenitor types discussed before.

Additionally, we estimate the age of the streams from typical velocities of the infalling progenitor, i.e., the velocity dispersion of the cluster ($\sim 1000 \text{ km s}^{-1}$), and their projected length. Our streams are between 10^8 and 5×10^8 yr old, which is only a rough estimate! However, as the streams are also red (Figure 9), triggered star formation by the merger is unlikely, as it would make them bluer. This circumstance opens the possibility for dwarf ellipticals (dEs) as progenitors for the "standard" and bright streams in our sample, as their total brightness would remain constant while the size increases.

Finally, we compare our streams to stream progenitors and Local Group dwarfs (see also Figure 40 in Patrick et al. 2022) in Figure 10. They analyzed streams in the galactic halo and measured their characteristic size, i.e., average width along the stream, and their absolute magnitude and linked them dwarf and GC progenitors. Our streams extend the distribution to the bright and wider end. We apply the same brightness argument, where in this Figure, for 75% of the streams, a local dwarf progenitor seems very unlikely, even if star formation would be induced during the stripping.

6.2. Connecting effective radius and width

The effective radius provides the remaining distinguishing factor between the (dwarf) Es and S0s. It is worth noting that the measurement of the effective width might be subject to temporal variability. That means the effective width of the stream depends on the current stage of the merger and the satellite stripping.

We do not know how exactly R_e behaves during and after the minor merger. There is an analysis by Er-rani et al. (2015), which uses high-resolution N -body simulations to trace the formation and evolution of

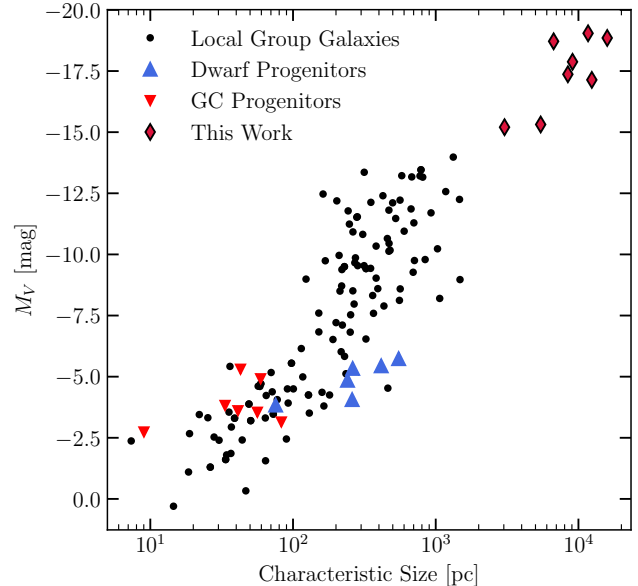


Figure 10. Characteristic size of tidal streams (triangles and diamonds) and known Local Group galaxies (black circles) against their total absolute V -band magnitude. The literature data (Local Group galaxies, GC progenitors, and dwarf progenitors) are taken from Patrick et al. (2022).

tidal streams across multiple pericentric passages coming from dwarf spheroidal galaxies. They found that the half-light radius of a stream increases with distance from the host galaxy based on the stripped particles at the pericenter. Generally this result supports our assumption of a constant or increasing R_e for this discussion. However, for our discussion, this also depends on the stripping stage of the stream, which we do not know. Hence, we do not discard the assumption of equal width for the discussion on possible progenitors.

In addition, simulations like the Illustris TNG50 (Nelson et al. 2019) predict the merging of lower-mass satellites with a larger host, while their stellar content gets stripped in the process. The emergence of multiple stellar streams is visible throughout the simulation. However, how the effective radius of the progenitor evolves during and after the stripping has not been studied to the extent that it is needed. We suspect that it depends on multiple variables, such as impact parameter, relative velocities, size, mass, position angle with respect to the major and minor axis radii, and the impact parameter.

6.3. Streams and Tails on the Red Sequence

For Tails, we neglect star-forming regions in our measurements. Prior to modeling, these regions are either masked or interpolated. As we measure fluxes, those missing pixels are replaced by the model. Given that newly formed stars tend to be bright and blue, the true

nature of the tails in Figure 9 is expected to be brighter and bluer. The magnitude of this effect depends on factors such as the number and size of star-forming regions. We do not quantify this effect. However, it was also shown in Mulia et al. (2015) that tails have diverse color ranges from red to blue colors depending on their host and the type of major merger.

All streams align with the red sequence of quiescent cluster members within a 2σ uncertainty. Those galaxies don't form stars by definition. While this would suggest that the streams in our sample originate from non-star-forming cluster members, the large error bars, especially in the color measurements from the LS, are also consistent with star-forming progenitors, or, perhaps, streams with triggered star formation caused by tidal forces. An improvement to distinguish between a passive and an active stream would be an analysis of the $u' - g'$ color. Unfortunately, the LS did not provide u -band observations. The WWFI Coma streams are covered by the u' -band but, there, the low S/N becomes increasingly more critical and makes the final $u' - g'$ color untrustworthy. An in-depth analysis is beyond the scope of this work.

In addition, we investigated the influence of the color in different aperture segments. We found that the scatter is consistent with the Poisson noise and background variations. The uncertainty of the local background has the strongest impact on the brightness measurements. We calculate the local background from a weighted average of the fitted Gaussian offsets. This average, however, is not able to capture variations in the background, e.g., in dense regions as for TS125926+275954 in the center of the coma cluster. For large streams with a lot of pixels, a small change in the choice of the local background can shift the colors of the feature by 0.1 mag. Other methods, such as background modeling and removal in inhomogeneous regions were not applied, and hence might improve those measurements, especially for those of the three streams in the Coma cluster.

7. SUMMARY

We have measured the properties of tidal streams and tails detected and classified in the Abell cluster sample in (Kluge et al. 2020, 2021). We utilize the DR10 from the Legacy Survey to complement our g' -band with g and r bands to obtain color information for each feature. A novel algorithm was developed to model these features and to create robust apertures, which were used for photometric analysis. The outputs of the stream modeling can be found in Appendix D, Figure 11 to 23. Our main findings are as follows:

1. Dwarf, lenticular, and (**dwarf**) elliptical galaxies are the proposed **progenitor** candidates for the streams in this work. For the three brightest streams, a progenitor of the latter two is more likely due to their brightness, which is a factor of 2 larger than the conservative definition of dwarf galaxies.
2. Streams are on average dimmer ($\overline{SB} \approx 26.25$ g' mag arcsec $^{-2}$) and redder ($(g' - r') \approx 0.70$ mag) than tails ($\overline{SB} \approx 25.14$ g' mag arcsec $^{-2}$ and $(g' - r') \approx 0.56$). This is in good agreement with the general classification and properties of major (tails) and minor mergers (streams).
3. We find that streams show sub-Milky Way luminosities with an average of $1.5 \times 10^9 L_{\odot}$.
4. The analyzed streams follow the red sequence of the Coma cluster within 2σ while located on the bright end relative to Coma member galaxies.
5. Tidal tails follow the same structural description as streams; namely, both can be described by 1D Gaussians with higher-order moments, perpendicular to their direction. At least, this is true for their faint underlying component.
6. Both streams and tails are efficiently modeled with our algorithm and with high accuracy of 7% for brightnesses or lower and 3% for the shape, regardless of the complexity of the stream.

8. ACKNOWLEDGMENTS

We thank the anonymous referee for providing comments and suggestions that allowed us to significantly improve the paper.

The Wendelstein 2.1 m telescope project was funded by the Bavarian government and by the German Federal government through a common funding process. Part of the 2.1 m instrumentation including some of the upgrades for the infrastructure were funded by the Cluster of Excellence ‘‘Origin of the Universe’’ of the German Science foundation DFG.

This paper uses data that were obtained by The Legacy Surveys: the Dark Energy Camera Legacy Survey (DECaLS; NOAO Proposal ID # 2014B-0404; PIs: David Schlegel and Arjun Dey), the Beijing-Arizona Sky Survey (BASS; NOAO Proposal ID # 2015A-0801; PIs: Zhou Xu and Xiaohui Fan), and the Mayall z -band Legacy Survey (MzLS; NOAO Proposal ID # 2016A-0453; PI: Arjun Dey). DECaLS, BASS, and MzLS together include data obtained, respectively, at the Blanco telescope, Cerro Tololo Inter-American Observatory,

National Optical Astronomy Observatory (NOAO); the Bok telescope, Steward Observatory, University of Arizona; and the Mayall telescope, Kitt Peak National Observatory, NOAO. NOAO is operated by the Association of Universities for Research in Astronomy (AURA) under a cooperative agreement with the National Science Foundation. Please see <http://legacysurvey.org> for details regarding the Legacy Surveys. BASS is a key project of the Telescope Access Program (TAP), which has been funded by the National Astronomical Observatories of China, the Chinese Academy of Sciences (the Strategic Priority Research Program "The Emergence of Cosmological Structures" Grant No. XDB09000000), and the Special Fund for Astronomy from the Ministry of Finance. The BASS is also supported by the External Cooperation Program of Chinese Academy of

Sciences (Grant No. 114A11KYSB20160057) and Chinese National Natural Science Foundation (Grant No. 11433005). The Legacy Surveys imaging of the DESI footprint is supported by the Director, Office of Science, Office of High Energy Physics of the U.S. Department of Energy under Contract No. DE-AC02-05CH1123, and by the National Energy Research Scientific Computing Center, a DOE Office of Science User Facility under the same contract; and by the U.S. National Science Foundation, Division of Astronomical Sciences under Contract No. AST-0950945 to the National Optical Astronomy Observatory.

Software: Astropy (Collaboration et al. 2022), Photutils (Bradley et al. 2023), numpy (Harris et al. 2020), SciPy (Virtanen et al. 2020)

REFERENCES

- Ahn, C. P., Alexandroff, R., Allende Prieto, C., et al. 2012, *ApJS*, 203, 21, doi: [10.1088/0067-0049/203/2/21](https://doi.org/10.1088/0067-0049/203/2/21)
- Akeson, R. L., Armus, L., Bachelet, E., et al. 2019, The Wide Field Infrared Survey Telescope: 100 Hubbles for the 2020s, doi: [10.48550/arXiv.1902.05569](https://doi.org/10.48550/arXiv.1902.05569)
- Alam, S., Albareti, F. D., Allende Prieto, C., et al. 2015, *ApJS*, 219, 12, doi: [10.1088/0067-0049/219/1/12](https://doi.org/10.1088/0067-0049/219/1/12)
- Baggett, W. E., Baggett, S. M., & Anderson, K. S. J. 1998, *The Astronomical Journal*, 116, 1626, doi: [10.1086/300525](https://doi.org/10.1086/300525)
- Belokurov, V., Zucker, D. B., Evans, N. W., et al. 2006, *ApJL*, 642, L137, doi: [10.1086/504797](https://doi.org/10.1086/504797)
- Bender, R., Burstein, D., & Faber, S. M. 1992, *ApJ*, 399, 462, doi: [10.1086/171940](https://doi.org/10.1086/171940)
- Bender, R., Kormendy, J., Cornell, M. E., & Fisher, D. B. 2015, *ApJ*, 807, 56, doi: [10.1088/0004-637X/807/1/56](https://doi.org/10.1088/0004-637X/807/1/56)
- Bennett, C. L., Larson, D., Weiland, J. L., & Hinshaw, G. 2014, *ApJ*, 794, 135, doi: [10.1088/0004-637X/794/2/135](https://doi.org/10.1088/0004-637X/794/2/135)
- Bilicki, M., Jarrett, T. H., Peacock, J. A., Cluver, M. E., & Steward, L. 2014, *ApJS*, 210, 9, doi: [10.1088/0067-0049/210/1/9](https://doi.org/10.1088/0067-0049/210/1/9)
- Bonaca, A., Geha, M., Küpper, A. H. W., et al. 2014, *ApJ*, 795, 94, doi: [10.1088/0004-637X/795/1/94](https://doi.org/10.1088/0004-637X/795/1/94)
- Bradley, L., Sipőcz, B., Robitaille, T., et al. 2023, *astropy/photutils*, 1.10.0, Zenodo, doi: [10.5281/zenodo.7946442](https://doi.org/10.5281/zenodo.7946442)
- Bruzual, G., & Charlot, S. 2003, *MNRAS*, 344, 1000, doi: [10.1046/j.1365-8711.2003.06897.x](https://doi.org/10.1046/j.1365-8711.2003.06897.x)
- Bullock, J. S., & Johnston, K. V. 2005, *ApJ*, 635, 931, doi: [10.1086/497422](https://doi.org/10.1086/497422)
- Bilek, M., Duc, P.-A., Cuillandre, J.-C., et al. 2020, *MNRAS*, 498, 2138, doi: [10.1093/mnras/staa2248](https://doi.org/10.1093/mnras/staa2248)
- Chilingarian, I. V., & Zolotukhin, I. Y. 2012, *MNRAS*, 419, 1727, doi: [10.1111/j.1365-2966.2011.19837.x](https://doi.org/10.1111/j.1365-2966.2011.19837.x)
- Chonis, T. S., Martínez-Delgado, D., J., G. R., et al. 2011, *ApJ*, 142, 166, doi: [10.1088/0004-6256/142/5/166](https://doi.org/10.1088/0004-6256/142/5/166)
- Collaboration, A., Price-Whelan, A. M., Lim, P. L., et al. 2022, *ApJ*, 935, 167, doi: [10.3847/1538-4357/ac7c74](https://doi.org/10.3847/1538-4357/ac7c74)
- Conselice, C. J., Mundy, C. J., Ferreira, L., & Duncan, K. 2022, *ApJ*, 940, 168, doi: [10.3847/1538-4357/ac9b1a](https://doi.org/10.3847/1538-4357/ac9b1a)
- Crnojević, D., Sand, D. J., Spekkens, K., et al. 2016, *ApJ*, 823, 19, doi: [10.3847/0004-637X/823/1/19](https://doi.org/10.3847/0004-637X/823/1/19)
- den Brok, M., Peletier, R. F., Valentijn, E. A., et al. 2011, *MNRAS*, 414, 3052, doi: [10.1111/j.1365-2966.2011.18606.x](https://doi.org/10.1111/j.1365-2966.2011.18606.x)
- Desmons, A., Brough, S., & Lanusse, F. 2024, *MNRAS*, 531, 4070, doi: [10.1093/mnras/stae1402](https://doi.org/10.1093/mnras/stae1402)
- Dey, A., Schlegel, D. J., Lang, D., et al. 2019, *ApJ*, 157, 168, doi: [10.3847/1538-3881/ab089d](https://doi.org/10.3847/1538-3881/ab089d)
- Domínguez Sánchez, H., Martin, G., Damjanov, I., et al. 2023, *MNRAS*, 521, 3861, doi: [10.1093/mnras/stad750](https://doi.org/10.1093/mnras/stad750)
- Duc, P.-A., Cuillandre, J.-C., Karabal, E., et al. 2014, *MNRAS*, 446, 120, doi: [10.1093/mnras/stu2019](https://doi.org/10.1093/mnras/stu2019)
- Elmegreen, D. M., Elmegreen, B. G., Ferguson, T., & Mullan, B. 2007, *The Astrophysical Journal*, 663, 734, doi: [10.1086/518715](https://doi.org/10.1086/518715)
- Errani, R., Peñarrubia, J., & Tormen, G. 2015, *MNRAS: Letters*, 449, L46, doi: [10.1093/mnrasl/slv012](https://doi.org/10.1093/mnrasl/slv012)
- Fardal, M. A., Babul, A., Geehan, J. J., & Guhathakurta, P. 2006, *MNRAS*, 366, 1012, doi: [10.1111/j.1365-2966.2005.09864.x](https://doi.org/10.1111/j.1365-2966.2005.09864.x)
- Ferrarese, L., Côté, P., Jordán, A., Peng, E. W., et al. 2006, *ApJS*, 164, 334, doi: [10.1086/501350](https://doi.org/10.1086/501350)

- Fisher, D. B., & Drory, N. 2008, *ApJ*, 136, 773, doi: [10.1088/0004-6256/136/2/773](https://doi.org/10.1088/0004-6256/136/2/773)
- Flewelling, H. A., Magnier, E. A., Chambers, K. C., et al. 2020, *ApJS*, 251, 7, doi: [10.3847/1538-4365/abb82d](https://doi.org/10.3847/1538-4365/abb82d)
- Foster, C., Lux, H., Romanowsky, A. J., et al. 2014, *Monthly Notices of the Royal Astronomical Society*, 442, 3544, doi: [10.1093/mnras/stu1074](https://doi.org/10.1093/mnras/stu1074)
- Gavazzi, G., Donati, A., Cucciati, O., et al. 2005, *A&A*, 430, 411, doi: [10.1051/0004-6361:20034571](https://doi.org/10.1051/0004-6361:20034571)
- Gavazzi, G., Franzetti, P., Scodreggio, M., Boselli, A., & Pierini, D. 2000, *A&A*, 361, 863, doi: [10.48550/arXiv.astro-ph/0007411](https://doi.org/10.48550/arXiv.astro-ph/0007411)
- Gibbons, S. L. J., Belokurov, V., & Evans, N. W. 2014, *MNRAS*, 445, 3788, doi: [10.1093/mnras/stu1986](https://doi.org/10.1093/mnras/stu1986)
- Grebel, E. K., Gallagher III, J. S., & Harbeck, D. 2003, *The Astronomical Journal*, 125, 1926–1939, doi: [10.1086/368363](https://doi.org/10.1086/368363)
- Gu, M., Conroy, C., Law, D., et al. 2020, *ApJ*, 894, 32, doi: [10.3847/1538-4357/ab845c](https://doi.org/10.3847/1538-4357/ab845c)
- Harris, C. R., Millman, K. J., van der Walt, S. J., et al. 2020, *Nature*, 585, 357, doi: [10.1038/s41586-020-2649-2](https://doi.org/10.1038/s41586-020-2649-2)
- Ibata, R., Malhan, K., Martin, N., et al. 2021, *ApJ*, 914, 123, doi: [10.3847/1538-4357/abfcc2](https://doi.org/10.3847/1538-4357/abfcc2)
- Ibata, R., Malhan, K., Tenachi, W., et al. 2024, *ApJ*, 967, 89, doi: [10.3847/1538-4357/ad382d](https://doi.org/10.3847/1538-4357/ad382d)
- Ivezić, Z., Kahn, S. M., Tyson, J. A., et al. 2019, *ApJ*, 873, 111, doi: [10.3847/1538-4357/ab042c](https://doi.org/10.3847/1538-4357/ab042c)
- Jester, S., Schneider, D. P., Richards, G. T., et al. 2005, *ApJ*, 130, 873, doi: [10.1086/432466](https://doi.org/10.1086/432466)
- Karademir, G. S., Remus, R.-S., Burkert, A., et al. 2019, *MNRAS*, 487, 318, doi: [10.1093/mnras/stz1251](https://doi.org/10.1093/mnras/stz1251)
- Kirby, E. M., Jerjen, H., Ryder, S. D., & Driver, S. P. 2008, *The Astronomical Journal*, 136, 1866, doi: [10.1088/0004-6256/136/5/1866](https://doi.org/10.1088/0004-6256/136/5/1866)
- Kluge, M. 2020, PhD thesis, Ludwig-Maximilians University of Munich, Germany
- Kluge, M., Bender, R., Riffeser, A., & other. 2021, *ApJS*, 252, 27, doi: [10.3847/1538-4365/abcda6](https://doi.org/10.3847/1538-4365/abcda6)
- Kluge, M., Neureiter, B., Riffeser, A., et al. 2020, *ApJS*, 247, 43, doi: [10.3847/1538-4365/ab733b](https://doi.org/10.3847/1538-4365/ab733b)
- Koposov, S. E., Erkal, D., Li, T. S., et al. 2023, *MNRAS*, 521, 4936, doi: [10.1093/mnras/stad551](https://doi.org/10.1093/mnras/stad551)
- Koposov, S. E., Rix, H.-W., & Hogg, D. W. 2010, *ApJ*, 712, 260, doi: [10.1088/0004-637X/712/1/260](https://doi.org/10.1088/0004-637X/712/1/260)
- Kormendy, J., & Bender, R. 2012, *ApJS*, 198, 2, doi: [10.1088/0067-0049/198/1/2](https://doi.org/10.1088/0067-0049/198/1/2)
- Kormendy, J., Fisher, D. B., Cornell, M. E., & Bender, R. 2009, *ApJS*, 182, 216, doi: [10.1088/0067-0049/182/1/216](https://doi.org/10.1088/0067-0049/182/1/216)
- Kosyra, R., Gössl, C., & Hopp, U. o. 2014, *Experimental Astronomy*, 38, doi: [doi:10.1007/s10686-014-9414-1](https://doi.org/10.1007/s10686-014-9414-1)
- Lahén, N., Johansson, P. H., Rantala, A., Naab, T., & Frigo, M. 2018, *Monthly Notices of the Royal Astronomical Society*, 475, 3934, doi: [10.1093/mnras/sty060](https://doi.org/10.1093/mnras/sty060)
- Laine, S., Martínez-Delgado, D., Webb, K. A., et al. 2024, *ApJ*, 962, 111, doi: [10.3847/1538-4357/ad16e4](https://doi.org/10.3847/1538-4357/ad16e4)
- Laine, S., Grillmair, C. J., Capak, P., et al. 2016, *The Astronomical Journal*, 152, 72, doi: [10.3847/0004-6256/152/3/72](https://doi.org/10.3847/0004-6256/152/3/72)
- Lauer, T. R., Postman, M., Strauss, M. A., Graves, G. J., & Chisari, N. E. 2014, *ApJ*, 797, 82, doi: [10.1088/0004-637X/797/2/82](https://doi.org/10.1088/0004-637X/797/2/82)
- Laurikainen, E., Salo, H., Buta, R., Knapen, J. H., & Comerón, S. 2010, *MNRAS*, 405, 1089, doi: [10.1111/j.1365-2966.2010.16521.x](https://doi.org/10.1111/j.1365-2966.2010.16521.x)
- Ledlow, M. J., & Owen, F. N. 1995, *AJ*, 109, 853, doi: [10.1086/117328](https://doi.org/10.1086/117328)
- Lotz, J. M., Jonsson, P., Cox, T. J., et al. 2011, *ApJ*, 742, 103, doi: [10.1088/0004-637X/742/2/103](https://doi.org/10.1088/0004-637X/742/2/103)
- Mahdavi, A., & Geller, M. J. 2004, *ApJ*, 607, 202, doi: [10.1086/383458](https://doi.org/10.1086/383458)
- Makarova, L. 1999, *A&AS*, 139, 491, doi: [10.1051/aas:1999402](https://doi.org/10.1051/aas:1999402)
- Malhan, K., & Ibata, R. A. 2019, *MNRAS*, 486, 2995, doi: [10.1093/mnras/stz1035](https://doi.org/10.1093/mnras/stz1035)
- Martin, N. F., Ibata, R. A., Starkenburg, E., et al. 2022, *Monthly Notices of the Royal Astronomical Society*, 516, 5331–5354, doi: [10.1093/mnras/stac2426](https://doi.org/10.1093/mnras/stac2426)
- Martínez-Delgado, D., Cooper, A. P., Román, J., et al. 2023a, *A&A*, 671, A141, doi: [10.1051/0004-6361/202245011](https://doi.org/10.1051/0004-6361/202245011)
- Martínez-Delgado, D., Peñarrubia, J., Gabany, R. J., et al. 2008, *ApJ*, 689, 184, doi: [10.1086/592555](https://doi.org/10.1086/592555)
- Martínez-Delgado, D., Roca-Fàbrega, S., Miró-Carretero, J., et al. 2023b, *A&A*, 669, A103, doi: [10.1051/0004-6361/202244832](https://doi.org/10.1051/0004-6361/202244832)
- Martínez-Delgado, D., Román, J., Erkel, D., et al. 2021, *MNRAS*, 506, 5030, doi: [10.1093/mnras/stab1874](https://doi.org/10.1093/mnras/stab1874)
- Mateo, M. 1998, *ARA&A*, 36, 435, doi: [10.1146/annurev.astro.36.1.435](https://doi.org/10.1146/annurev.astro.36.1.435)
- Mateu, C. 2023, *Monthly Notices of the Royal Astronomical Society*, 520, 5225, doi: [10.1093/mnras/stad321](https://doi.org/10.1093/mnras/stad321)
- McConnachie, A. W., Ibata, R., Martin, N., et al. 2018, *ApJ*, 868, 55, doi: [10.3847/1538-4357/aae8e7](https://doi.org/10.3847/1538-4357/aae8e7)
- McConnachie, A. W., & Irwin, M. J. 2006, *MNRAS*, 365, 1263, doi: [10.1111/j.1365-2966.2005.09806.x](https://doi.org/10.1111/j.1365-2966.2005.09806.x)
- Miró-Carretero, J., Martínez-Delgado, D., Farràs-Aloy, S., et al. 2023, *A&A*, 669, L13, doi: [10.1051/0004-6361/202245003](https://doi.org/10.1051/0004-6361/202245003)

- Mouhcine, M., Ibata, R., & Rejkuba, M. 2010, *ApJL*, 714, L12, doi: [10.1088/2041-8205/714/1/L12](https://doi.org/10.1088/2041-8205/714/1/L12)
- Mulia, A. J., Chandar, R., & Whitmore, B. C. 2015, *The Astrophysical Journal*, 805, 99, doi: [10.1088/0004-637X/805/2/99](https://doi.org/10.1088/0004-637X/805/2/99)
- Nelson, D., Springel, V., Pillepich, A., et al. 2019, *Computational Astrophysics and Cosmology*, 6, 2, doi: [10.1186/s40668-019-0028-x](https://doi.org/10.1186/s40668-019-0028-x)
- Nibauer, J., Bonaca, A., & Johnston, K. V. 2023, *ApJ*, 954, 195, doi: [10.3847/1538-4357/ace9bc](https://doi.org/10.3847/1538-4357/ace9bc)
- Pace, A. B. 2024, arXiv e-prints, arXiv:2411.07424, doi: [10.48550/arXiv.2411.07424](https://doi.org/10.48550/arXiv.2411.07424)
- Padilla, N. D., & Strauss, M. A. 2008, *Monthly Notices of the Royal Astronomical Society*, 388, 1321, doi: [10.1111/j.1365-2966.2008.13480.x](https://doi.org/10.1111/j.1365-2966.2008.13480.x)
- Patrick, J. M., Kuposov, S. E., & Walker, M. G. 2022, *MNRAS*, 514, 1757, doi: [10.1093/mnras/stac1478](https://doi.org/10.1093/mnras/stac1478)
- Pildis, R. A., Schombert, J. M., & Eder, J. A. 1997, *The Astrophysical Journal*, 481, 157, doi: [10.1086/304040](https://doi.org/10.1086/304040)
- Price-Whelan, A. M., Hogg, D. W., Johnston, K. V., & Hendel, D. 2014, *ApJ*, 794, 4, doi: [10.1088/0004-637X/794/1/4](https://doi.org/10.1088/0004-637X/794/1/4)
- Richards, F. 2022, PhD thesis, Swansea University, doi: <https://doi.org/10.23889/SUthesis.62601>
- Rines, K. J., Geller, M. J., Diaferio, A., & Hwang, H. S. 2016, *ApJ*, 819, 63, doi: [10.3847/0004-637X/819/1/63](https://doi.org/10.3847/0004-637X/819/1/63)
- Román, J., Rich, M. R., Ahvazi, N., et al. 2023, *A&A*, doi: [10.48550/arXiv.2305.03073](https://doi.org/10.48550/arXiv.2305.03073)
- Román, J., Trujillo, I., & Montes, M. 2020, *A&A*, 644, A42, doi: [10.1051/0004-6361/201936111](https://doi.org/10.1051/0004-6361/201936111)
- Ryden, B. S. 1996, *ApJ*, 461, 146, doi: [10.1086/177043](https://doi.org/10.1086/177043)
- Sanders, J. L., & Binney, J. 2013, *Monthly Notices of the Royal Astronomical Society*, 433, 1826, doi: [10.1093/mnras/stt816](https://doi.org/10.1093/mnras/stt816)
- Scaramella, R., Amiaux, J., Mellier, Y., et al. 2022, *A&A*, 662, A112, doi: [10.1051/0004-6361/202141938](https://doi.org/10.1051/0004-6361/202141938)
- Schechter, P. 1976, *ApJ*, 203, 297, doi: [10.1086/154079](https://doi.org/10.1086/154079)
- Schulze, F., Remus, R.-S., Dolag, K., et al. 2020, *MNRAS*, 493, 3778, doi: [10.1093/mnras/staa511](https://doi.org/10.1093/mnras/staa511)
- Sola, E., Duc, P.-A., Richards, F., et al. 2022, *A&A*, 662, A124, doi: [10.1051/0004-6361/202142675](https://doi.org/10.1051/0004-6361/202142675)
- Tammann, G. A. 1994, in *European Southern Observatory Conference and Workshop Proceedings*, Vol. 49, European Southern Observatory Conference and Workshop Proceedings, 3
- Tonry, J. L., Stubbs, C. W., Lykke, K. R., et al. 2012, *The Astrophysical Journal*, 750, 99, doi: [10.1088/0004-637X/750/2/99](https://doi.org/10.1088/0004-637X/750/2/99)
- Toomre, A., & Toomre, J. 1972, *ApJ*, 178, 623, doi: [10.1086/151823](https://doi.org/10.1086/151823)
- Urbano, M., Duc, P. A., Saifollahi, T., et al. 2024, arXiv e-prints, arXiv:2412.17672, doi: [10.48550/arXiv.2412.17672](https://doi.org/10.48550/arXiv.2412.17672)
- Virtanen, P., Gommers, R., Oliphant, T. E., et al. 2020, *Nature Methods*, 17, 261, doi: [10.1038/s41592-019-0686-2](https://doi.org/10.1038/s41592-019-0686-2)
- Wenger, M., Ochsenbein, F., Egret, D., et al. 2000, *A&AS*, 143, 9, doi: [10.1051/aas:2000332](https://doi.org/10.1051/aas:2000332)
- Willmer, C. N. A. 2018, *ApJS*, 236, 47, doi: [10.3847/1538-4365/aabfdf](https://doi.org/10.3847/1538-4365/aabfdf)
- Wright, E. L. 2006, *Publications of the Astronomical Society of the Pacific*, 118, 1711, doi: [10.1086/510102](https://doi.org/10.1086/510102)
- Yu, N., Ho, L. C., Wang, J., & Li, H. 2022, *ApJS*, 261, 21, doi: [10.3847/1538-4365/ac626b](https://doi.org/10.3847/1538-4365/ac626b)
- Zöller, R., Kluge, M., Staiger, B., & Bender, R. 2024, *ApJS*, 271, 52, doi: [10.3847/1538-4365/ad2775](https://doi.org/10.3847/1538-4365/ad2775)

APPENDIX

A. MODELING ALGORITHM

We conducted extensive testing to evaluate the performance and quality of our modeling algorithm. Owing to its low computational cost, our algorithm is well suited for automated pipelines handling large datasets. Although some manual intervention is required, these tasks can also be automated. For instance, the selection of the position and size of the initial box could be trained using a neural network, which may already be employed to identify such features in vast fields. Alternatively, it could be used to determine the centroid of a polygon-like segmentation mask, also provided by a neural network.

Our algorithm does have its limitations. Features with pronounced curvature in a projected view, particularly those observed at low inclination angles, cannot be effectively modeled. This is because we treat the angle fit parameter as to be constant in the cutout feature segment. For parts with strong curvature, this assumption does not hold. Room for improvement lies in the behavior of the modeling box. Currently, it remains either vertical or horizontal, whereas employing a rotating box could enhance the modeling process by ensuring that the box remains perpendicular to the orientation of the feature.

We also emphasize that our intrinsic best-fit parameters are those for an assumed circular Gaussian PSF. However, as asymmetric PSFs exist, and PSFs are often described by other forms, e.g., Moffat profile, using the true PSF of the image would result in the true intrinsic shape of the feature. Although, we suspect that this change will only slightly change the fit parameters.

B. THE GAUSSIAN BOX FRAMEWORK

In the following, we describe how a Gaussian is fitted to a 2D finite box with a width $W \equiv 2w + 1$ and a height $H \equiv 2h + 1$. Both can be expressed in terms of ranges, for example, the width ranges from $-h$ to h . With that, we construct two vectors \vec{x} and \vec{y} representing the horizontal and vertical dimensions of the box, respectively.

$$\vec{x}(w) = [-w \ \dots \ w], \vec{y}(h) = \begin{bmatrix} h \\ \vdots \\ -h \end{bmatrix} w, h \in \mathbb{Z} \quad (\text{B1})$$

Not only do they have the same corresponding dimensions for the sides of the box, but encapsulate distance information, i.e., each value in these vectors directly

represents the pixel distance from the center. When stacking \vec{x} vertically and \vec{y} horizontally, we end up with two matrices with the same dimensions as the box ($\dim(\mathbf{x}) = \dim(\mathbf{y}) = 2h + 1 \times 2w + 1$).

$$\mathbf{x} = \text{vstack}\{\vec{x}\} = \begin{bmatrix} -w & \dots & w \\ \vdots & \ddots & \vdots \\ -w & \dots & w \end{bmatrix} \quad (\text{B2})$$

$$\mathbf{y} = \text{hstack}\{\vec{y}\} = \begin{bmatrix} h & \dots & h \\ \vdots & \ddots & \vdots \\ -h & \dots & -h \end{bmatrix} \quad (\text{B3})$$

By adding both matrices together, we get a distance grid, where each pixel stores the information of its distance to a certain "zeroth" line. The idea behind it is that when feeding the grid into a Gaussian function, the "zeroth" line transforms to values of one, while the rest distributes themselves symmetrically around the mean (when taking a 1D slice).

$$\Delta = \mathbf{x} + \mathbf{y} = \begin{bmatrix} -w + h & \dots & w + h \\ \vdots & \ddots & \vdots \\ -w - h & \dots & w - h \end{bmatrix} \quad (\text{B4})$$

To allow for a grid rotation and translation, the simple addition is modified by angle and offset parameters. Our grid is now constructed so that an angle of zero translates into a fully vertical stream segment with its orientation angle increasing counterclockwise.

$$\Delta(\mathbf{x}, \mathbf{y}, x_0, y_0, \alpha) = \cos(\alpha)(x - x_0) + \sin(\alpha)(y - y_0) \quad (\text{B5})$$

To create a stream segment, the grid is inserted into a Gaussian function. As **described in Section 3.3.2** the Gaussian is extended to higher-order moments utilizing the Hermite basis functions and a cumulative distribution function. With this setup, every imaginable stream segment can be constructed with a total of nine fit parameters. They vary along the stream track and build up the entire structural description of the stream (or tail).

C. 76-98-99.9 RULE

Here we derive the analog to the 68–95–99.7 rule for the FWHM criterion. The standard deviation and the FWHM are connected via

$$\text{FWHM} = 2\sqrt{2 \ln 2} \sigma \approx 2.3548\sigma. \quad (\text{C6})$$

But the FWHM describes, as the name suggests, the full width; hence, the direct transformation from σ only needs the half-width at half-maximum (HWHM).

$$\text{HWHM} \equiv \lambda = \sqrt{2 \ln 2} \sigma \approx 1.1774 \sigma. \quad (\text{C7})$$

To find the percentage of the full area under a Gaussian distribution, we first assume a normalized Gaussian.

$$P(x, \mu, \sigma) = \frac{1}{\sqrt{2\pi}\sigma} \exp\left(-\frac{1}{2}\left(\frac{x-\mu}{\sigma}\right)^2\right) \quad (\text{C8})$$

Now we integrate the function inside the borders.

$$\frac{1}{\sqrt{2\pi}\sigma} \int_{\mu-n\sigma}^{\mu+n\sigma} \exp\left(-\frac{1}{2}\left(\frac{x-\mu}{\sigma}\right)^2\right) dx \quad (\text{C9})$$

By substituting $u = \frac{x-\mu}{\sigma}$, along $dx = \frac{1}{\sigma} du$ and $\mu \pm n\sigma \Rightarrow \pm n$ the integral simplifies to

$$\frac{1}{\sqrt{2\pi}} \int_{-n}^n \exp\left(-\frac{1}{2}u^2\right) du. \quad (\text{C10})$$

Since we do not want to integrate from $-n$ to n , which would give us the area in steps of σ , we have to further substitute our definition for it, i.e., multiplying $\pm n$ by $\sqrt{2 \ln 2}$.

$$\frac{1}{\sqrt{2\pi}} \int_{-\sqrt{2 \ln 2} n}^{\sqrt{2 \ln 2} n} \exp\left(-\frac{1}{2}u^2\right) du. \quad (\text{C11})$$

At the end, choosing $n \in \{1, 2, 3\}$ we arrive at

$$P(\mu - 1\lambda \leq X \leq \mu + 1\lambda) \approx 0.7610 \quad (\text{C12})$$

$$P(\mu - 2\lambda \leq X \leq \mu + 2\lambda) \approx 0.9815 \quad (\text{C13})$$

$$P(\mu - 3\lambda \leq X \leq \mu + 3\lambda) \approx 0.9996 \quad (\text{C14})$$

forming the 76–98–99.9 rule, where λ is the HWHM.

D. STREAM AND TAIL MODELS

We provide the streams, their models, the masks, the residuals, and the μ_1 apertures in Figure 11 to 23.

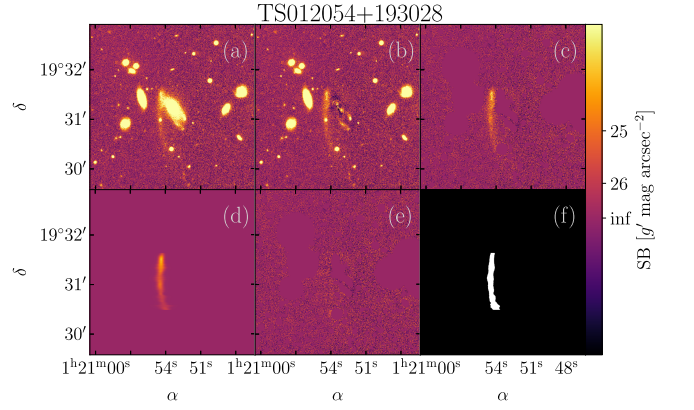


Figure 11. Visualization of the TS012054+193028 stream. (a) The original image cutout. (b) Image after subtracting an isophotal galaxy model. (c) **Source mask** multiplied onto panel (b). (d) The model created by ASTROSTREAMPY. (e) The residual image. (f) The μ_1 aperture.

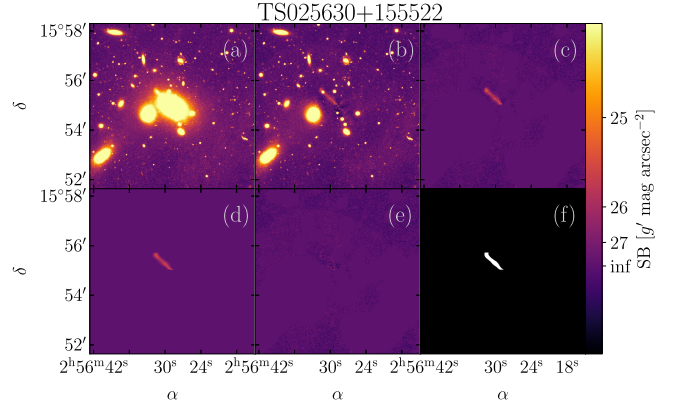


Figure 12. Same as in Figure 11 but for the TS025630+155522 stream.

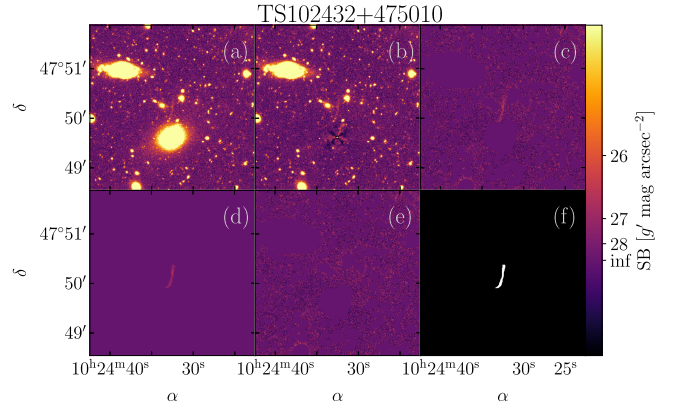


Figure 13. Same as in Figure 11 but for the TS102432+475010 stream.

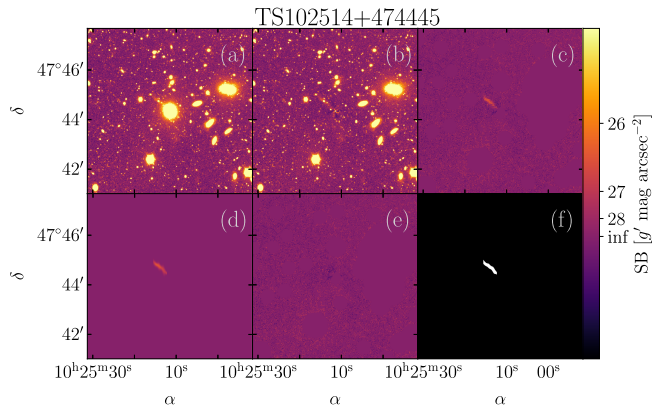


Figure 14. Same as in Figure 11 but for the TS102514+474445 stream.

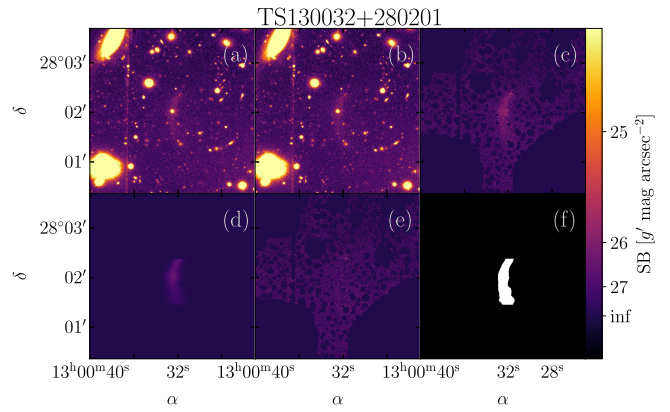


Figure 17. Same as in Figure 11 but for the TS130032+280201 stream and without subtracting an isophotal model.

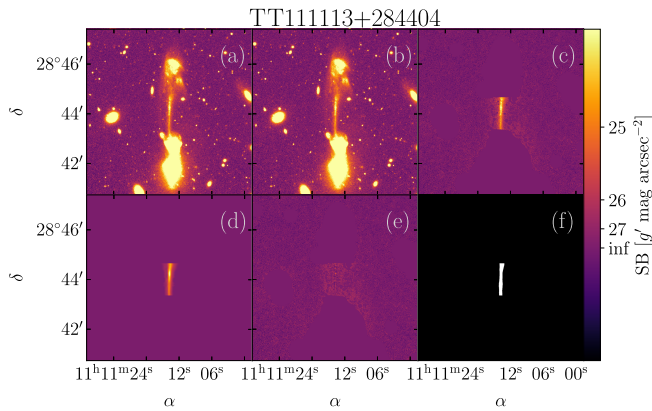


Figure 15. Same as in Figure 11 but for the TT111113+284404 tail and without subtracting an isophotal model.

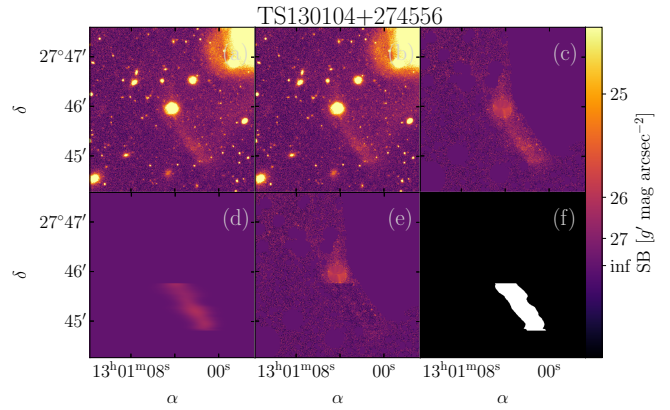


Figure 18. Same as in Figure 11 but for the TS130104+274556 stream and without subtracting an isophotal model.

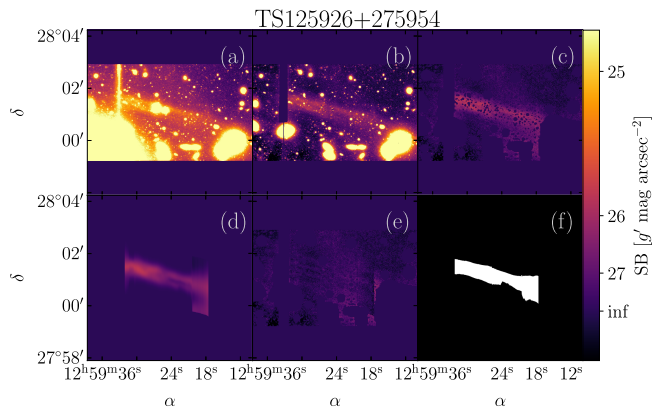


Figure 16. Same as in Figure 11 but for the TS125926+275954 stream and with subtracting four galaxy models in total. Two of those are the BCGs not visible anymore in the final cutout.

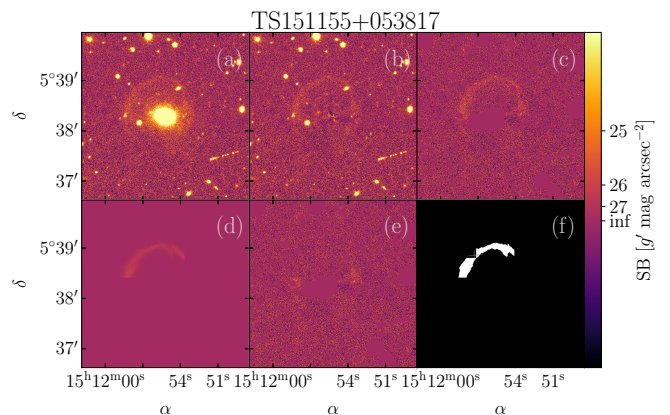


Figure 19. Same as in Figure 11 but for the TS151155+053817 stream.

E. CLASSIFIED TIDAL FEATURES

Table 4 and 5 contain all tidal features identified and classified during the WWFI Abell g' -band manual image

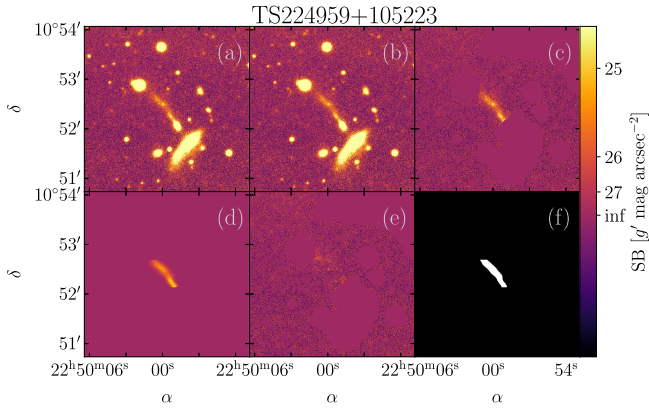


Figure 20. Same as in Figure 11 but for the TS224959+105223 stream and without subtracting an isophotal model.

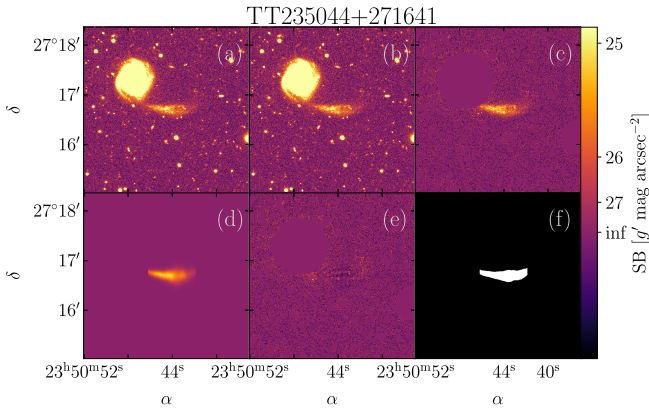


Figure 21. Same as in Figure 11 but for the TT235044+271641 tail and without subtracting an isophotal model.

inspection. The ones used in the analysis of this paper are not listed but found in Table 1. Features separated by '/' indicate an OR case, where '&' means that both features are present in the image. The classified features were also cross checked with their appearance in the Legacy Survey DR10 to help with the classification using color information.

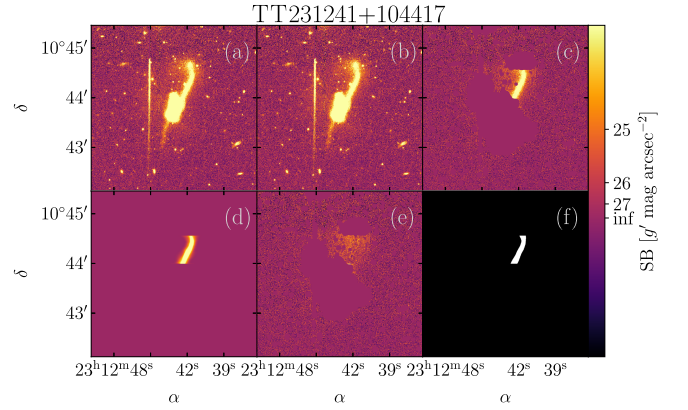
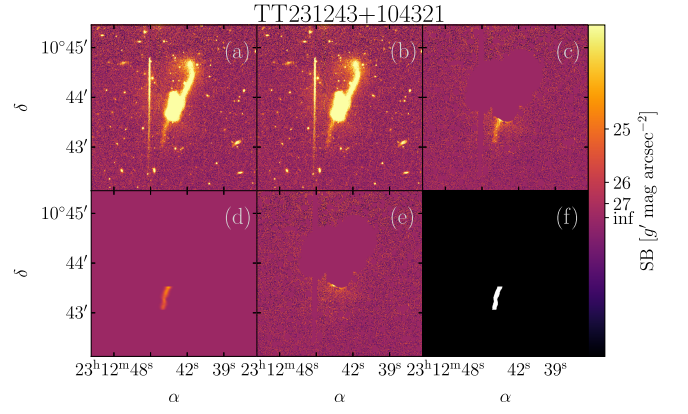


Figure 22. Same as in Figure 11 but for the tails TT231243+104321 and TT231241+104417 and without subtracting an isophotal model.

α_{Feature} J2000 (1)	δ_{Feature} J2000 (2)	z_{Feature} (3)	z Candidate (4)	Angular Scale [kpc/''] (5)	Feature (6)
17.878888	17.457995	-	2MASX J01113078+1727282	-	Tail&Stream
17.882192	17.609381	-	2MASX J01113133+1736353	-	Shell
25.813381	6.554159	-	-	-	Stream
26.225615	6.382950	0.0918310	LAMOST J014453.48+062301.0	1.721	Stream/Tail
27.283573	14.221135	0.1227400	LEDA 1452449	2.221	Stream/Tail
27.285417	13.962861	0.0705500	2MASX J01490841+1357474	1.355	Shell
27.451133	13.846310	0.0438800	2MASX J01494842+1350450	0.869	Stream
44.154073	13.004558	0.0660620	2MASX J02563682+1300191	1.275	Stream/Shell
79.270523	6.172417	0.0423890	UGC 3278	0.841	Tail
93.569523	48.378326	-	-	-	Tail/Spiral Arm
100.091940	69.967313	-	LEDA 2733304	-	Tail/Spiral Arm
116.044925	9.234112	0.0609625	2MASX J07441076+0914036	1.184	Shell
117.355476	52.043750	0.0683000	MCG+09-13-062	1.315	Stream/Tail
118.188519	29.405885	0.0549480	NVSS J075245+292419	1.075	Stream/Tail/Spiral Arm
118.504914	29.420762	0.0360400	LEDA 1865757	0.721	Stream/Tail/Spiral Arm
118.506025	29.437427	0.1022400	LEDA 1866269	1.894	Tail
123.665965	58.222177	0.0268800	UGC 4281	0.543	Tail/Merger
123.936703	58.321017	0.0270500	UGC 4289	0.547	Shell
127.182836	30.405352	0.0526200	IC 2380	1.032	Shell
127.422200	30.688373	0.0476200	IC 2383	0.939	Shell
136.910766	16.592621	0.0729300	2MASX J09073872+1635334	1.397	Shell
147.979809	5.712064	0.0732700	LEDA 1287878	1.403	Stream/Tail
156.801606	10.984194	0.0337522	2MASX J10271185+1059573	0.677	Tail
157.091027	10.727597	0.2014100	SDSSCGB 8207.1	3.344	Tail
159.021312	41.421745	0.1198300	LEDA 2180848	2.176	Tail/Spiral Arm
159.025891	41.453541	0.1202100	2MASS J10360603+4126022	2.182	Stream
159.502640	41.764194	0.1199130	2MASX J10380107+4145534	2.177	Tail
164.940379	10.796817	0.0386400	LEDA 33115	0.770	Stream/Tail
165.188659	10.568083	0.0338400	IC 664	0.679	Stream
168.101120	39.613875	0.0750600	LEDA 2152868	1.434	Tail/Spiral Arm
169.081513	29.253911	0.0452800	NVSS J111622+291507	0.896	Stream/Tail
171.703864	35.249622	0.0322500	Mrk 423	0.648	Tail
172.297598	54.116694	0.0683700	2MASX J11291167+5407028	1.316	Tail
175.461621	10.276678	0.1188600	2MASX J11415073+1016340	2.160	Stream&Tail
175.520162	10.339691	0.0207400	NGC 3819	0.422	Stream
175.529333	10.147528	0.1187900	2MASX J11420742+1008578	2.159	Stream
175.692387	10.301782	0.1179100	SDSS J114246.57+101813.4	2.145	Tail/Ring Spiral Arm
176.225352	19.778392	0.0274200	2MASX J11445486+1946349	0.554	Shell
176.275089	19.794546	0.067*	2MASX J11450584+1947329	1.292	Stream
176.287225	19.812583	0.0684894	[CGB2004b] J114509+194845	1.319	Stream
176.322840	20.021520	0.0177720	2MASX J11451755+2001106	0.363	Merger
177.778368	55.078017	0.0196800	NGC 3921	0.401	Tail
178.516940	23.340012	0.0509300	LEDA 37330	1.001	Tail/Spiral Arm
179.354138	33.678161	0.1261600	SDSS J115724.81+334043.5	2.274	Tail/Spiral Arm
180.735731	51.696392	0.0630886	2MASX J12025666+5141437	1.222	Stream/Shell/Tail
180.747194	51.827954	0.2863400	NVSS J120259+514947	4.349	Tail/Spiral Arm
180.821093	51.402197	0.0296610	Mrk 1465	0.598	Merger
184.954941	5.464035	0.0079605	NGC 4270	0.165	Shell

Table 4. List of Tidal Features Found in the WWFI Abell cluster sample. All redshifts were determined with SIMBAD (Wenger et al. 2000). The R.A. and decl. are given in degrees.

α_{Feature} J2000 (1)	δ_{Feature} J2000 (2)	z_{Feature} (3)	z Candidate (4)	Angular Scale [kpc/''] (5)	Feature (6)
185.426955	13.755289	0.0825200	LEDA 169111	1.563	Stream/Tail
191.829224	30.020983	0.1386200	SDSS J124719.29+300123.6	2.465	Stream/Merger
195.233755	27.791371	0.0265900	NGC 4911	0.538	Shell
197.758424	39.192192	0.0781500	2MASX J13110199+3911281	1.488	Tail
202.488028	37.295658	0.0554320	2MASX J13295738+3717447	1.084	Tail
203.610585	59.374177	0.0721900	SDSS J133432.04+592156.8	1.384	Stream
204.035015	59.206639	0.0733812	MCG+10-19-096	1.405	Shell
207.360545	26.461400	0.0763800	2MASX J13492678+2627426	1.457	Shell&Stream
207.421321	26.717214	0.0665700	3XMM J134941.2+264301	1.285	Tail/Stream/Shell
208.276422	5.151083	0.0788500	2MASX J13530637+0508586	1.500	Shell
209.540299	18.341026	0.0631700	2MASX J13580938+1820217	1.224	Tail/Spiral Arm
209.672206	20.302733	0.064*	LEDA 1623208	1.239	Tail/Spiral Arm
209.749308	28.068404	0.0628100	LEDA 93770	1.217	Stream/Spiral Arm
215.258601	17.699847	0.0512600	IC 1004	1.007	Shell
215.375845	17.571912	0.0509200	LEDA 1535967	1.001	Tail
216.535770	16.788718	0.0873100	2MASX J14260855+1647167	1.645	Stream&Tail
222.718011	30.524442	0.0608100	LEDA 1907325	1.181	Stream
222.813522	30.474584	0.1629800	2MASX J14511539+3028213	2.821	Tail
227.746036	5.743472	0.0891800	LEDA 54175	1.676	Tail/Spiral Arm
229.188233	7.176194	0.1033615	2MASX J15164535+0710330	1.912	Tail&Merger
230.325925	30.833527	0.0740800	2MASX J15211835+3049584	1.417	Shell/Spiral Arm
230.593450	27.557305	0.0732700	2MASX J15222245+2733262	1.403	Stream/Tail
230.640788	27.644913	0.0638800	2MASX J15223389+2738441	1.236	Shell
240.532971	15.697583	0.0344500	IC 1165b	0.690	Tail
240.551719	15.908417	0.0357900	MCG+03-41-051	0.716	Shell
240.887740	16.323267	0.0381030	MCG+03-41-061	0.760	Shell
241.247652	17.871129	0.0331900	NGC 6044	0.666	Shell
241.388719	17.595926	0.0339800	IC 1181	0.681	Tail
241.404705	17.802575	0.0352136	IC 1182	0.705	Shell&Stream
241.418981	18.057720	0.0400500	LEDA 1548961	0.797	Tail
241.672458	16.320024	0.0367190	UGC 10204	0.734	Shell/Tail
242.937131	29.748091	0.0508100	LEDA 200332	0.999	Tail
242.991003	29.837605	0.0500680	UGC 10262	0.985	Shell
255.702219	78.742003	0.0669963	2MASX J17024809+7844270	1.292	Shell
290.633032	44.059785	0.0493070	2MASX J19223199+4403385	0.971	Stream
340.051613	12.177075	-	-	-	Stream
340.113598	12.361590	-	-	-	Stream/Ring
345.275320	18.879946	0.0341336	2MASX J23010596+1852475	0.684	Tail
354.251329	20.651082	0.0578250	SDSS J233658.90+203910.1	1.127	Tail/Merger
354.273366	15.933285	0.0660700	LEDA 1496749	1.276	Tail/Spiral Arm
354.325872	15.938152	0.1467600	SDSS J233717.91+155616.1	2.586	Stream/Merger
354.463773	20.961078	0.0700284	LEDA 1639646	1.346	Tail/Spiral Arm
354.622946	27.033706	0.0303543	NGC 7720	0.611	Shell
354.672522	15.955254	0.0133500	NGC 7722	0.274	Shell
354.727457	21.489628	0.0551300	LEDA 1651104	1.078	Tail
358.994947	11.615024	0.0707550	LEDA 1396212	1.359	Stream
359.007999	11.688415	0.0720680	LEDA 1397303	1.382	Tail/Stream
359.019950	11.066182	0.075*	-	1.433	Stream/Tail

Table 5. Continued list of WWFI tidal features of Table 4.

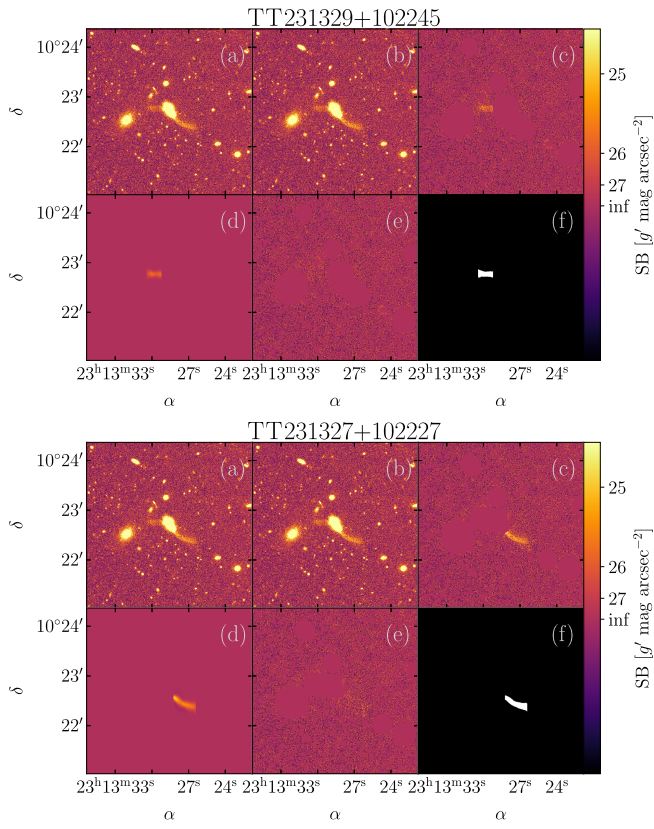


Figure 23. Same as in Figure 11 but for the tails TT231329+102245 and TT231327+102227 and without subtracting an isophotal model.